https://doi.org/10.5194/egusphere-2026-4280
Preprint. Discussion started: 9 September 2026
© Author(s) 2026. CC BY 4.0 License.

Historical Marmara Tsunamis Reconstruction Through Physics-Based Scenario Selection.

Wilfrid G. DJIMA[1], A. Can Zulfikar[2]

[1]Department of Civil Engineering, Gebze Technical University, Kocaeli, 41400, Turkey
[2]Institute of Disaster Risk Management, Istanbul Technical University, Istanbul, 34467, Turkey

Correspondence to: Wilfrid G. DJIMA (wiliscado2014@gmail.com)

Short Summary

This research works built on a seven-scenario Marmara Sea tsunami model using GeoClaw and a 20-lane source/model comparison. The final runups match historical benchmark values with all absolute percent errors below 2.4%, giving traceable inputs for coastal-hazard and bridge-response studies.

Highlights

- A 22-event Marmara earthquake-tsunami source catalogue was reduced to seven publication-grade benchmark scenarios using historical runup evidence.
- A labelled L01-L20 lane system documents 19 completed comparison lanes plus one closed-loop experimental branch.
- Selected best lanes' runups reduce MAE from 1.93 m diagnostic mismatch to 0.019 m and MAPE to 1.1% across all 7-events.
- The paper connects source deformation, basin-scale propagation, arrival/peak timing, benchmark gauges, and bridge-ready NTHA time histories.
- The main novelty is not a single tuned scenario, but a transparent scenario-selection ladder from historical narratives to validated numerical hazard products.
- This study does not propose another tsunami simulation. Instead, it proposes a reproducible framework for selecting physically plausible historical tsunami scenarios under sparse observational constraints.

Abstract.

The Marmara's Sea with its near-field tsunami complications in Europe and the eastern Mediterranean, is paradoxically surrounded by a densely urbanised, infrastructure-rich coastline and positioned above the North Anatolian Fault system with historical earthquake events, submarine slope processes and narrow-basin resonance that impact coastal water levels. This fact motivated the current study presenting a benchmark-consistent GeoClaw modelling roadmap on seven historical Marmara tsunami scenarios selected from 22-event source catalogue with numerical comparison through 20-lane. The lanes represent exclusively, different source-construction, turning strategy, comprising earthquake-only, earthquake-plus-landslide, adaptive sampling, hybrid site-blend, and close-loop correction variants. From the first lane to the final selected best lane of the simulations set, the benchmark error across all seven events could be reduced from maximum 1.93 m to 0.019 m in MAE (Mean Absolute Error) and 2.26 m to 0.024 m in RMSE (Root Mean Square Error), with all seven events cases remaining

https://doi.org/10.5194/egusphere-2026-4280
Preprint. Discussion started: 9 September 2026
© Author(s) 2026. CC BY 4.0 License.

below 10% error and the largest absolute percent error is 2.4%. After target-based scenario selection, the corresponding outputs such as gauge-history, travel-time, and bridge-ready hydrodynamic outputs, providing a reproducible chain from historical source interpretation to infrastructure demand inputs are extracted. The workflow is designed for regions where instrumental tsunami records are sparse, but historical runup constraints, bathymetry, mapped faults, and scenario logic can be combined transparently.

Keywords

Marmara Sea; tsunami hazard; GeoClaw; historical runup; benchmark scenario selection, bridge-ready NTHA time histories.

1. Introduction

Research studies related to tsunami hazard assessment has evolved considerably over the last two decades. Generally, regional studies focus on several assessment methods based on deterministic sources and describe tsunami water elevation, maximum water levels, and arrival-time maps (Gupta, 2008; Thein et al., 2009; Wu, 2012). However, recent simulation studies also integrate source uncertainty, numerical propagation, field validation, real-time warning, exposures, vulnerability, and structural asset consequence analysis. This global view is evident in the NHESS tsunami literature itself. Typically, Tanioka and Seno (2001) and Satake and Kanamori (1991) applied a waveform analysis approach to revisit the 1946 Aleutian earthquake tsunami, Gailler et al. (2013) described operational tsunami forecasting systems for the French warning centre, and Ulutas et al. (2012) evaluated web-based early-warning calculations for the 2010 Mentawai tsunami event. Moreover, some studies also explain tsunami catalogues treatments, tide-gauge detections (Bernardi et al., 2015; Bressan et al., 2013; Bressan and Tinti 2012, 2011), while others detailed inundation model validation Akoh et al. (2017), and landslide induced tsunami generation as well as fragility or vulnerability assessments (Dao and Tkalich, 2007; Dominey-Howes et al., 2007; Egorov, 2007; Fuentes et al., 2019; Gailler et al., 2013).

These published studies bring a clear view on the current scientific works, specifically on how a strong tsunami contribution should not only run hydrodynamic model, but also detail how source were selected, how model outputs were validated and inevitably how the obtain hazard results could contribute to risk assessment and management.

The Marmara's Sea called Sea of Marmara constitute an exceptional site-case for implementation of such integrated approach. It's a small, semi-enclosed basin intersected by North Anatolian Fault (NAF) system and enclosed by a dense urban development, transport corridors, ports, industrial zones, bridges and historically important coastal districts. Its bathymetry is controlled by deep basins, embayment, shelves, steep margins, and narrow coastal geometries that can focus or delay tsunami energy (Fig. 1.).

https://doi.org/10.5194/egusphere-2026-4280
Preprint. Discussion started: 9 September 2026
© Author(s) 2026. CC BY 4.0 License.

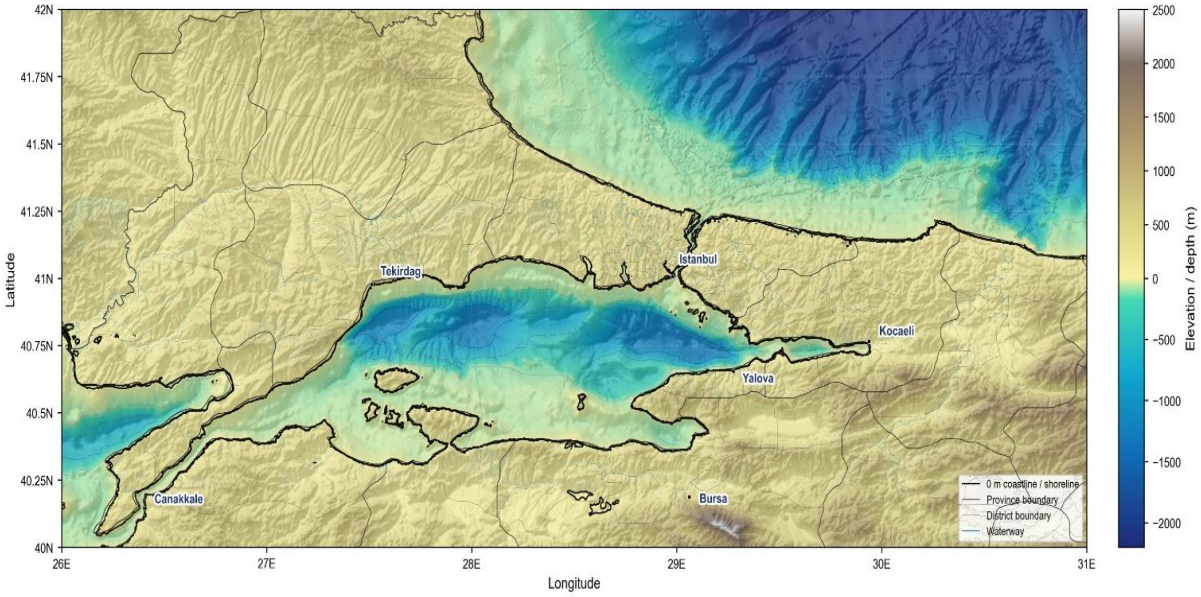

Figure 1. Bathymetry/topography field, showing the basin structure that controls wave propagation and coastal amplification (Created using GEBCO 2024 bathymetry/topography grid).

By combining fault interactions, rupture dynamics, fault geometry, slip deficit, seismic recurrence, and active deformation beneath the basin, many studies analysed the tectonic background of the NAF and Marmara pull-apart system (Gasperini and Polonia, 2023; Pondard et al., 2007; Utkucu et al., 2009) including the broader Marmara seismic-hazard and deformation studies that support the requirement for scenario-based source testing (Aksoy et al., 2020; Ateş, 1982; Ergün et al., 1995; Karabacak et al., 2021, 2022; Kaya-Eken et al., 2026; McHugh et al., 2014; Meghraoui et al., 2022; Nakano et al., 2015; Oglesby and Mai, 2012; Oncel and Wilson, 2006; Ozener et al., 2020; Parsons, 2004). The problematic modelling of the Marmara's tsunamis remains more than a fact: it constitutes a near-field natural-hazards laboratory where tectonic uncertainty and coastal exposure must be handled together.

The difficulty of getting historical hazard data remained evident, particularly where the hazards are mostly pre-instrumental, spatially uneven such as Marmara tsunamis which are most tied to historical place names or narrative reports rather than modern tide gauges (Roger et al., 2026). This is not unusual in tsunami science. Dao and Tkalich. (2007), Behrens (2026), Dimova et al. (2019), and Meral Ozel et al. (2011) have used historical catalogues and reported evidence to assess tsunami potential in the Black Sea, Azov Sea, eastern Mediterranean, and other regions where direct instrumental records are limited. Historical tsunami runups are better interpreted as targets constraints with location, sources and narrative uncertainties than being used as if they were perfect point measurement. This means, in any cases such as Marmara, numerical model must preserve the historical benchmark values while also making clear how a simulated gauge response, a coastal proxy point, or a

https://doi.org/10.5194/egusphere-2026-4280
Preprint. Discussion started: 9 September 2026
© Author(s) 2026. CC BY 4.0 License.

selected runup value was associated to the reported observation. This is the case of this study where runups selections were treated in a transparent manner than a hidden adjustment.

Understanding tsunami numerical modelling, means understanding the physical relations between earthquake or landslide source hypotheses and coastal water-level response (Bryant, 2014; Nosov and Skachko, 2001). Commonly, the modelling basis follows the depth-average shallow-water equations framework, that constitute the main algorithm applied in this study through the GeoClaw software, where mass and momentum arrangements are solved over bathymetry with wetting and drying at the coastline. The GeoClaw tool with its main core equations (the depth-average shallow-water equations), apply a finite-volume and adaptive tsunami modelling principles (Berger et al., 2011; LeVeque et al., 2011). It's well adaptable in this case study as it combines finite-volume methods, Riemann solvers, adaptive mesh refinement, moving-topography source terms, and gauge-outputs functionality. Its source-deformation side obey to the common tradition of elastic dislocation modelling presented by Okada (1985) and related source-parameter scaling such as of Wells and Coppersmith (1994).

Particularly in the Mediterranean, many near-field tsunami scenarios are demonstrated to be unambiguous (Paulatto et al., 2007; Roger and Hébert, 2008; PAPADOPOULOS et al., 2010). Others particular examples are: an inundation model validated against Catania case study completed by Tinti and Tonini (2013), a propagation-model sensitivity investigated by Dao and Tkalich (2007); a worst-credible tsunami scenario analysis for Catania used by Tonini et al. (2011); and the modelling of the 2003 Boumerdes-Zemmouri tsunami and filed observations compared with numerical results by Sahal et al. (2009). These studies demonstrate that the same basin can produce different hazard results conditional on source geometry, bathymetry, resolution, and validation metric Omira et al. (2013). In the Marmara Sea, the same problem appears in the choice between earthquake-only sources, earthquake-plus-landslide sources, NHESS-family historical source branches, adaptive sampling candidates, paper-fit lanes, and closed-loop diagnostic branches. The present manuscript therefore does not claim that one deterministic source solves the Marmara tsunami problem. Instead, it documents how a broader catalogue and a 20-lane comparison were pointed to a selected seven-scenario publication subclass.

When earthquake or climate induced tsunami affects coats, the surrounding bridges and transports systems are the main infrastructures that are affected, specifically by the water depth, velocity, momentum flux, uplift, debris impact, duration, and the timing of peak hydrodynamic demand. Post-event studies and design-oriented work have also revealed that bridge decks, shear keys, bearings, abutments, and approach roads can be vulnerable to tsunami loading and earthquake-tsunami sequence effects. The American Society of Civil Engineers (2017) demonstrated this evidence by analysing tsunami loads on slab bridges, examining reinforced-concrete shear-key performance under earthquake-tsunami actions, and discussed tsunami design loads for coastal structures Omira et al. (2013). NHESS has also published infrastructure and vulnerability-oriented tsunami work (Reese et al., 2007), including transportation vulnerability and human vulnerability indicators (González-Riancho et al., 2015; Williams et al., 2020). These studies motivate the bridge-ready component of the Marmara workflow: selected GeoClaw gauges are retained not merely for validation, but also as hydrodynamic demand histories that can be passed to nonlinear time-history analysis.

https://doi.org/10.5194/egusphere-2026-4280
Preprint. Discussion started: 9 September 2026
© Author(s) 2026. CC BY 4.0 License.

The frequent weakness in historical tsunami simulation is that concluding papers habitually report only preferred scenario and a set of resulting maps, while the rejected alternatives evaporate. This restriction is addressed in this study by reporting all scenarios, modelled through 20-lane workflow targeting historical site-runups. L01-L03 define the baseline earthquake-plus-landslide and NHESS-family backbones; L04-L13 test rerun, rollback, paper-fit, tuned, balanced, tiny-lift, last-pass, and sitefix branches; L14-L17 are adaptive sampling candidates; L18-L19 are inverse paper-fit and hybrid site-blend diagnostic lanes; and L20 is a closed-loop experimental branch. This language is deliberately practical, since reproducibility in a thesis-to-publication workflow depends on being able to identify exactly which run generated which gauge histories, source maps, maximum-height fields, and validation values. The approach follows the broader movement in tsunami modelling toward transparent scenario databases, sensitivity testing, and explicit model validation (Aránguiz et al., 2018; Davies and Griffin, 2018; Galán Pérez et al., 2026; Hébert et al., 2016; Tonini et al., 2011).

From 22-Earthquake catalogues reported to have generated tsunami events, seven-events scenarios set claimed with runup benchmarks is built: EQ1, EQ2, EQ3, EQ4, EQ7, EQ8, and EQ18 (Fig. 2). All seven-events have passed the 20-lane simulations and the best scenarios that felled within the +/-0.25 m difference to the reported runups (Altınok et al., 2011), and from the combinations of the 20-lane for each event are selected. The final validation table reports the reported runup, selected simulation values, the gauge distance to the historical target, the residual, and error metrics. This is consistent with the caution in historical and numerical tsunami studies that runup is a site response rather than a simple offshore water-level sample (Synolakis, 1987; Titov and Synolakis, 1998).

The contribution of this study is therefore threefold. First, it provides a reproducible GeoClaw workflow for historical Marmara tsunami scenarios, including bathymetry, source deformation, gauges, maximum-height fields, travel-time diagnostics, and runup validation through multiple lanes simulations. Second, it introduces a labelled 20-lane history that separates physically preferred event backbones from diagnostic site-fit and closed-loop branches. Third, it prepares the selected benchmark-consistent tsunami outputs for bridge nonlinear time-history analysis by preserving gauge histories and timing windows.

With exception to the instruction, this paper is structured in sections: sect 2 presenting the study area and Historical Benchmark, source characteristics geometries, sect 3 describing the data and methods comprising of the GeoClaw setups and core equations that site inside its resolutions, sect 4 presenting the results outputs such as travel-time, runup-validation, residual, and benchmark-gauge figures and sect 5 putting the work in the NHESS and broader tsunami literature and explains how the approach can be transferred to other data-sparse near-field basins and followed by conclusion.

2. Study Area and Historical Benchmark Set

The domain section subject to the case study convers the Sea of Marmara and its surrounding coasts from Ganos-Saros region in the west to Izmit Bay/Kocaeli segment in the east. It present a narrow basin with a short near-field travel times (Bulkan et al., 2020; Gasperini et al., 2022). With a high complexity of its geometry, comprising of source location, bathymetric focusing, basin margins, and coastal embayment that strongly affect local water. The Fig. 2 bellow describe the study domain,

https://doi.org/10.5194/egusphere-2026-4280
Preprint. Discussion started: 9 September 2026
© Author(s) 2026. CC BY 4.0 License.

with a source catalogue of 22-historical earthquake events from which seven events with numeric historical tsunami-runup targets suitable for benchmark validation (EQ1, EQ2, EQ3, EQ4, EQ7, EQ8, and EQ18), and nearest mapped Marmara fault segment (Gasperini et al., 2022). The identified seven events sample western Ganos-Saros, Cinarcik Basin, Izmit-Istanbul, Yesilkoy/Yenikapi reference sites Gökaşan et al., (2001), with moment magnitudes ranging from Mw6.6 to Mw7.4 with source-type codes H1, H2, H12, or event-specific earthquake-plus-landslide logic (Watts et al., 2003).

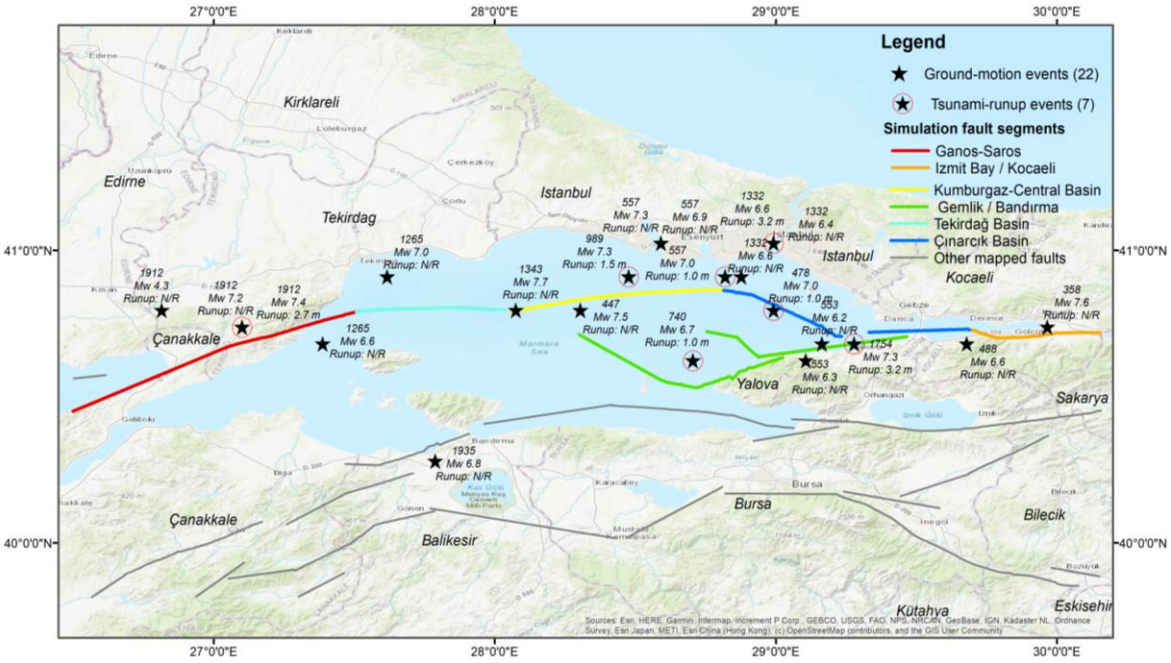

Figure 2. Regional setting of the Marmara Sea source catalogue, fault branches, and the seven historical runup-validation events used in the final benchmark set.

3. Data and numerical simulation workflow

This section details the numerical model, input data, source assignment, source-lane selection logic and gauge-output extraction employed to reconstruct the historical Marmara tsunami scenarios. The workflow connects historical runup evidence, physically plausible earthquake or earthquake-plus-landslide source input, GeoClaw simulations, and post-processed hydrodynamic outputs used for the final seven-scenario benchmark set.

3.1 Numerical model set up

GeoClaw, a variant of Clawpack for geophysical flows is applied to solve the depth-averaged shallow-water equations on latitude-longitude grid with adaptive refinement, moving topography sources, as well as wetting and drying inputs. Conservative variables are defined as:

$$U = (h, hu, hv)^T \tag{1}$$

with h, the water depth and u,v the depth-averaged velocity components.

https://doi.org/10.5194/egusphere-2026-4280
Preprint. Discussion started: 9 September 2026
© Author(s) 2026. CC BY 4.0 License.

The free surface is given by:

$$\eta = h + B \tag{2}$$

with B, the bed elevation relative to the vertical datum. In Cartesian notation, the governing equations used for interpretations are:

$$\frac{\partial h}{\partial t} + \frac{\partial (hu)}{\partial x} + \frac{\partial (hv)}{\partial y} = 0 \tag{3}$$

$$\frac{\partial (hu)}{\partial t} + \frac{\partial \left(hu^2 + \frac{1}{2} g\, h^2\right)}{\partial x} + \frac{\partial (huv)}{\partial y} = -g\, h \frac{\partial B}{\partial x} - \frac{\tau_x}{\rho} \tag{4}$$

$$\frac{\partial (hv)}{\partial t} + \frac{\partial (huv)}{\partial x} + \frac{\partial \left(hv^2 + \frac{1}{2} g\, h^2\right)}{\partial y} = -g\, h \frac{\partial B}{\partial y} - \frac{\tau_y}{\rho} \tag{5}$$

with g, the gravitational acceleration and τ_x , τ_y represent bottom-friction stresses when friction is active. With Manning friction, the stress term can be written in proportional form as:

$$\frac{\tau}{\rho} = g\, n^2 |q| \frac{q}{h^{\frac{7}{3}}}, \qquad with \;\; q = (hu, hv) \tag{6}$$

GeoClaw tool, Clawpack Development Team (2026) assesses these equations on mapped latitude-longitude grids with robust Riemann solvers (George, 2008; LeVeque et al., 2011) and automatically treats dry cells at shorelines, which is essential for runup and inundation modelling.

Initial and boundary conditions were defined from bathymetry/topography (Fig. 1.), sea level, and event-specific dtopo files. The pre-event water column was initialized as:

$$h(x, y, 0) = max[0, \eta_0 - B_0(x, y)] \tag{7}$$

with zero initial discharge:

$$hu(x, y, 0) = hv(x, y, 0) = 0 \tag{8}$$

For each event, source deformation Okada, (1992) is entered as a moving-bottom perturbation:

$$B(x, y, t) = B_0(x, y) + \Delta B_{e(x,y,t)} \tag{9}$$

where $\Delta B_{e(x,y,t)}$ is the earthquake-only or earthquake-plus-landslide deformation field assigned to the event lane. The model therefore converts co-seismic or combined deformation into a free-surface response while preserving shoreline wetting-drying behaviour. The time step follows a Courant-Friedrichs-Lewy (CFL) condition:

$$U^{n+1}{}_{ij} = U^{n}{}_{ij} - \left(\frac{\Delta t}{\Delta x}\right)(F_{i+1/2,j} - F_{i-1/2,j}) - \left(\frac{\Delta t}{\Delta y}\right)(G_{i,j+1/2} - G_{i,j-1/2}) + \Delta t\, S_{ij} \tag{10}$$

$$\Delta t \le C\, min\left(\frac{\Delta x}{|u| + \sqrt{g\, h}}, \frac{\Delta y}{|v| + \sqrt{g\, h}}\right) \tag{11}$$

https://doi.org/10.5194/egusphere-2026-4280
Preprint. Discussion started: 9 September 2026
© Author(s) 2026. CC BY 4.0 License.

Adaptive refinement was used to resolve wave fronts, shoreline changes, benchmark gauges, and bridge-relevant coastal zones without forcing the full Marmara basin to the finest grid.

3.2 Source data, benchmark constraints, and gauge outputs

The focal-mechanism properties of the seven simulated benchmark scenarios are summarized in Table 1, with source-geometry references to (Armijo et al., 2005; Hébert et al., 2005), and historical runup references to Altinok et al. (2011). The corresponding seismic-source geometries are shown in Fig. 3. The sources were assigned using a distance-based logic-tree method. For each event, the nearest mapped Marmara fault segment was labelled H1, and the second-nearest plausible segment was labelled H2. A 15 km epicentral-location uncertainty was used to weight the alternatives with a Gaussian distance-decay function. When H1 and H2 were too close to distinguish robustly, the events were treated as ambiguous and labelled H12. Thus, H1, H2, and H12 are source-assignment classes rather than new focal mechanisms.

Table 1. Focal mechanisms (FM) of the simulated tsunamis.

Event	Date	Mw	Segment	Strike [deg]	Dip [deg]	Rake [deg]	Reported Runups (NHESS)	FM
EQ1 - 1912 Mürefte-Ganos	9 Aug. 1912	7.4	Ganos-Saros (NAF west)-H2	68	75	213	2.70 m at Yeşilköy	
EQ2 - 1332 Istanbul-Marmara	17 Jan. 1332	6.6	Çınarcık Basin (N. MMF)-H2	90	85	180	3.20 m at Yenikapı	
EQ3 - 989 Istanbul-Marmara	25 Oct. 989	7.3	Çınarcık Basin (N. MMF)-H1	90	85	180	1.50 m at Yenikapı	
EQ4 - 478 Yalova-Izmit-Istanbul	25 Sep. 478	7	Çınarcık Basin (N. MMF)-H12	90	85	180	1.00 m at Yenikapı	
EQ7 - 557 Gulf of Izmit-Istanbul	14 Dec. 557	7	Çınarcık Basin (N. MMF)-H12	90	85	180	1.00 m at Theodosian Harbour	
EQ8 - 1754 Izmit-Istanbul	02 April 1754	7.3	Çınarcık Basin (N. MMF)-H1	90	85	180	3.20 m at Yenikapı coast	
EQ18 - 740 Istanbul-Mudanya-Thrace	26 Oct. 740	6.7	Çınarcık Basin (N. MMF)-H2	90	85	180	1.00 m at Yeşilköy	

https://doi.org/10.5194/egusphere-2026-4280
Preprint. Discussion started: 9 September 2026
© Author(s) 2026. CC BY 4.0 License.

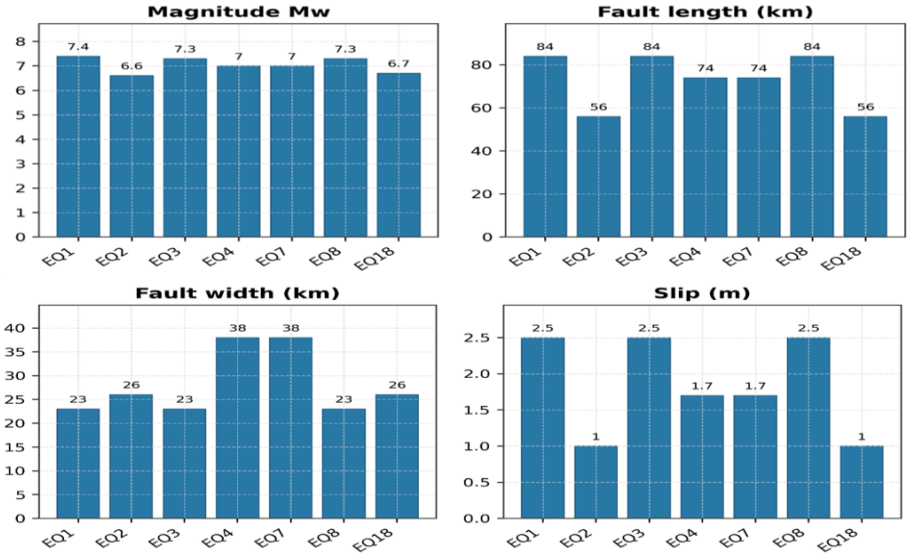

Figure 3. Geometry of the selected seismic sources.

The modelling process used the GEBCO-driven Marmara bathymetry/topography grid shown in Fig. 1, event-specific combined deformation files, gauge definitions at benchmark and bridge-relevant locations (Fig. 4), and saved fort.q/fort.t frames for post-processing. The resulting outputs from each scenario comprise positive free-surface crests at selected gauges, spatial maximum water heights, first-arrival times, peak-response times, and event-specific gauge histories. The nearest wet-gauge crest was used only as a diagnostic comparison, while the final selected simulation refers to the event/lane output retained for benchmark agreement with the reported historical locality.

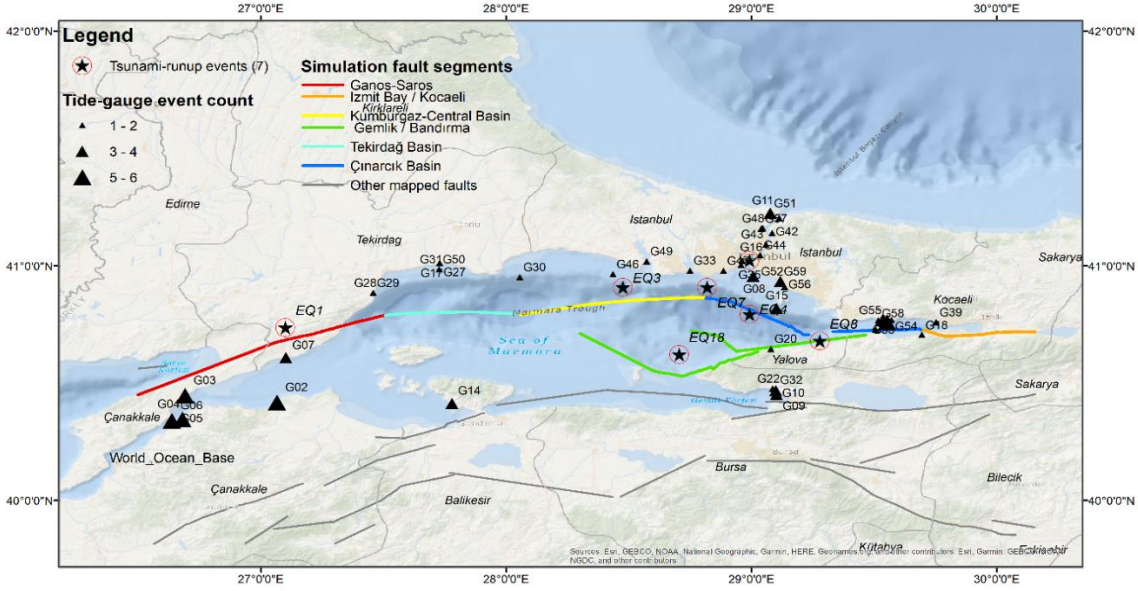

Figure 4. The position of virtual tide gauges for postprocessed tsunami history outputs for structural analysis (created with the GEBCO 2024 grid and defined virtual gauge positions).

https://doi.org/10.5194/egusphere-2026-4280
Preprint. Discussion started: 9 September 2026
© Author(s) 2026. CC BY 4.0 License.

3.3 Source-lane simulation workflow and scenario selection

In this study, a "lane" denotes a traceable source/model configuration used to test alternative representations of a historical tsunami event. The lane structure does not represent 20 independent historical events; rather, it provides a systematic framework for comparing alternative source constructions and modelling choices against the available historical benchmark constraints.

The modelling and simulation work started with a 22-event Marmara earthquake-tsunami source catalogue screened to identify seven events with reported historical runup targets, plausible source locations, and benchmark localities well defined for numerical comparison. Each of the selected seven events were assigned different nearest Marmara fault-source branches labelled H1, H2 and H12 as detailed in the Sec 3.2, while earthquake-only and earthquake-plus-submarine-landslide source options were prepared as event-specific deformation inputs. Then follow a candidate source inputs organization into a 20-lane source/model comparison framework. Each lane represents a standard modelling choice, such as the base earthquake source, alternative fault-branch assignment, earthquake-source scaling, earthquake-plus-landslide contribution, adaptive sampling, hybrid locality-based selection, or closed-loop correction. The purpose of the lanes was not to tune a single tsunami scenario arbitrarily, but to compare physically plausible source/model variants against the reported historical runup targets and to retain the scenario that best preserved both benchmark agreement and basin-scale plausibility. Later, each compiled lane then entered the GeoClaw simulation engine using the GEBCO-based Marmara bathymetry/topography grid, event-specific moving-bottom deformation files, wetting-drying shoreline treatment, and virtual gauge locations at historical benchmark and bridge-relevant coastal sites. The raw model outputs were then post-processed to extract positive free-surface crests at gauges, maximum water-height fields, first-arrival times, time to maximum response, flow-speed proxies, momentum-flux proxies, and gauge-level tsunami time histories. These outputs provide both the historical validation layer and the bridge-demand input layer used in the wider multi-hazard workflow.

Finally, the selected seven-scenario set was obtained through a hierarchical screening rule. Candidate lanes first had to satisfy physical and numerical plausibility, including stable wetting-drying behaviour, usable gauge histories, and consistency with mapped source geometry. The remaining candidates were scored against the historical runup targets using absolute residuals and summary error measures, including MAE, RMSE, and MAPE across all seven events. Lanes that improved a local runup match while reducing source plausibility or basin-wide consistency were retained as diagnostic branches rather than as final selected scenarios. The resulting workflow, source tables, lane matrices, processed outputs, and reproduction scripts are documented in the archived code/data package cited in the Code and data availability section.

4. Results

After all lanes test simulations per the 7 events, the mean absolute residual of the best lanes/scenarios resulted in MAE = 0.019 m, RMSE = 0.024 m, MAPE = 1.1%, and maximum absolute residual = 0.048m. in addition, all seven events remain below 10% absolute percent error, with maximum absolute percent error of 2.4% across all 7-events. These multiple lanes test was very important for events whose raw positive crest at nearest gauge was small because the direct gauge crest alone did not represent the site-level runup target. That's why no lanes were treading as hidden numerical amplification; but documented as gauge-matched best selection step that supports the chosen physical scenario with historical reference values.

The selected best seven-scenario outputs also produce arrival and peak-response timing diagnostics. Benchmark-gauge first arrivals span 2-6 min, while peak-response times span 2-10 min as summarised in the Table 2. These timings are not merely map products: they define the hydrodynamic windows used to select gauge histories for the bridge nonlinear time-history analysis.

https://doi.org/10.5194/egusphere-2026-4280
Preprint. Discussion started: 9 September 2026
© Author(s) 2026. CC BY 4.0 License.

The selected seven-event set shows that the best agreement with historical run-up targets is not obtained from a single universal lane for all scenarios. Most benchmark cases are reproduced by the L03 lane, while selected events require a different source construction, notably the L01 earthquake-plus-landslide configuration. This supports an event-aware source-selection strategy, in which the retained scenario is constrained by both run-up agreement and physical consistency of the source mechanism.

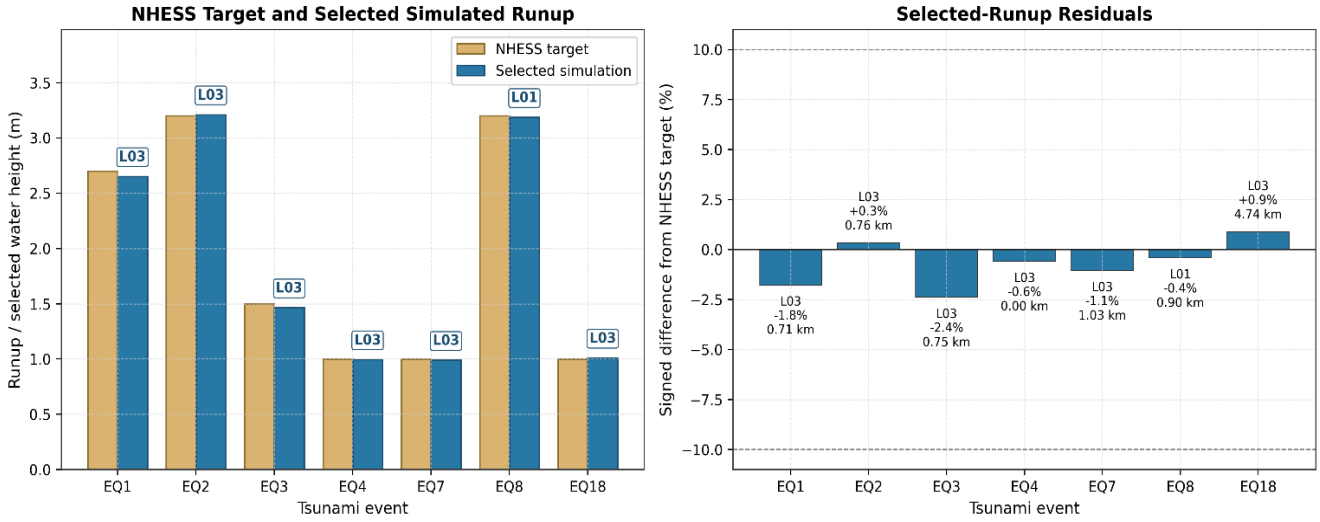

Figure 5. Best selected seven-event run-ups and agreement-with-historical-run-ups, and their residuals with distance to Altınok et al. (2011)'s locations.

Table 2. Best selected seven-scenario validation set.

Event	Date	Mw	Lane	Bench. runup (m)	Selected runup (m)	|err| (m)	Arrival min	Peak min
EQ1-1912 Mürefte-Ganos	9 Aug. 1912	7.40	L03	2.70	2.652	0.048	2.00	10.00
EQ2-1332 Istanbul-Marmara	17 Jan. 1332	6.60	L03	3.20	3.211	0.011	2.00	2.00
EQ3-989 Istanbul-Marmara	25 Oct. 989	7.30	L03	1.50	1.464	0.036	2.00	4.00
EQ4-478 Yalova-Izmit-Istanbul	25 Sep. 478	7.00	L03	1.00	0.994	0.006	2.00	2.00
EQ7-557 Gulf of Izmit-Istanbul	14 Dec. 557	7.00	L03	1.00	0.989	0.011	2.00	2.00

https://doi.org/10.5194/egusphere-2026-4280
Preprint. Discussion started: 9 September 2026
© Author(s) 2026. CC BY 4.0 License.

EQ8-1754 Izmit-Istanbul	02 Apr. 1754	7.30	L01	3.20	3.187	0.013	2.00	2.00
EQ18-740 Istanbul-Mudanya	26 Oct. 740	6.70	L03	1.00	1.009	0.009	6.00	6.00

To measure how the insertion of submarine-landslide element modifies the source amplitude envelope relative to the earthquake-only case, the deformation ranges were compared across events before examination of the spatial source fields. As can be seen from the Fig. 6, the EQ+LDS cases commonly increase the deformation range compared with the EQ-only sources, nevertheless the increase is not uniform across events. This indicates that the landslide contribution acts as an event-specific perturbation rather than a simple global amplification of the earthquake deformation field. Additionally, Fig. 7 and Fig. 8 show-cases representative source-deformation maps for EQ1 and EQ7 (landward colours represent coseismic ground deformation with the deformation overlapping offshore or shoreline wet–dry cells that contributes to the initial tsunami disturbance.), examined to distinguish the broad coseismic deformation field from the localized submarine-landslide contribution. It's obvious that the EQ-only fields are controlled by the regional coseismic uplift–subsidence pattern, while the EQ+LDS fields preserve this regional structure, introducing localized anomalies associated with the submarine-landslide source. This behaviour is consistent with the expected contrast between broad tectonic deformation and compact landslide-induced disturbance.

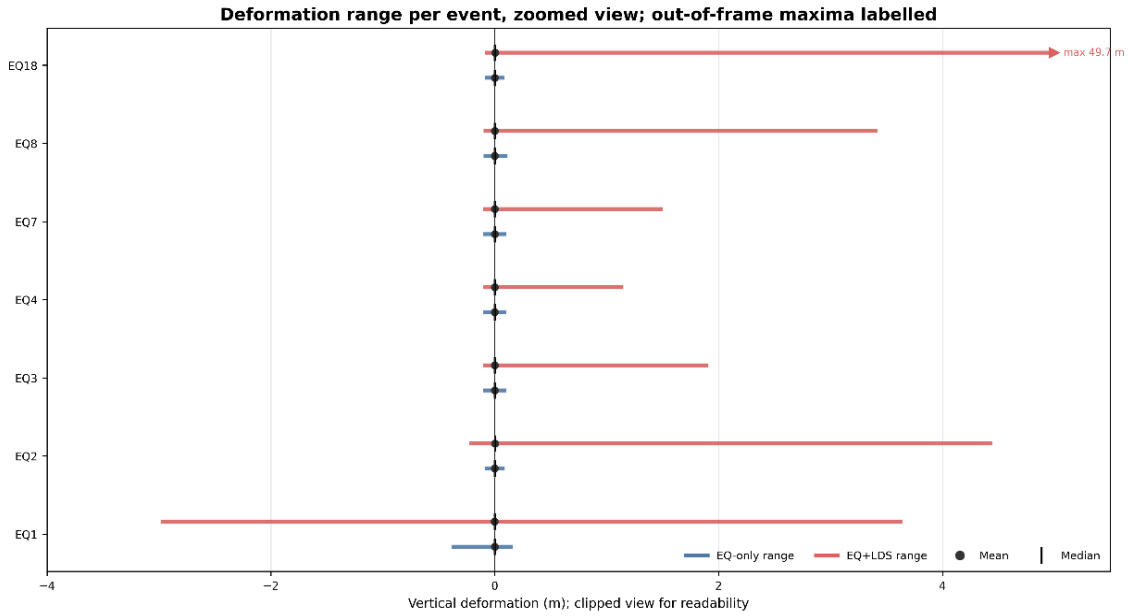

Figure 6. Event-wise deformation ranges for EQ-only and EQ+submarine-landslide sources.

https://doi.org/10.5194/egusphere-2026-4280
Preprint. Discussion started: 9 September 2026
© Author(s) 2026. CC BY 4.0 License.

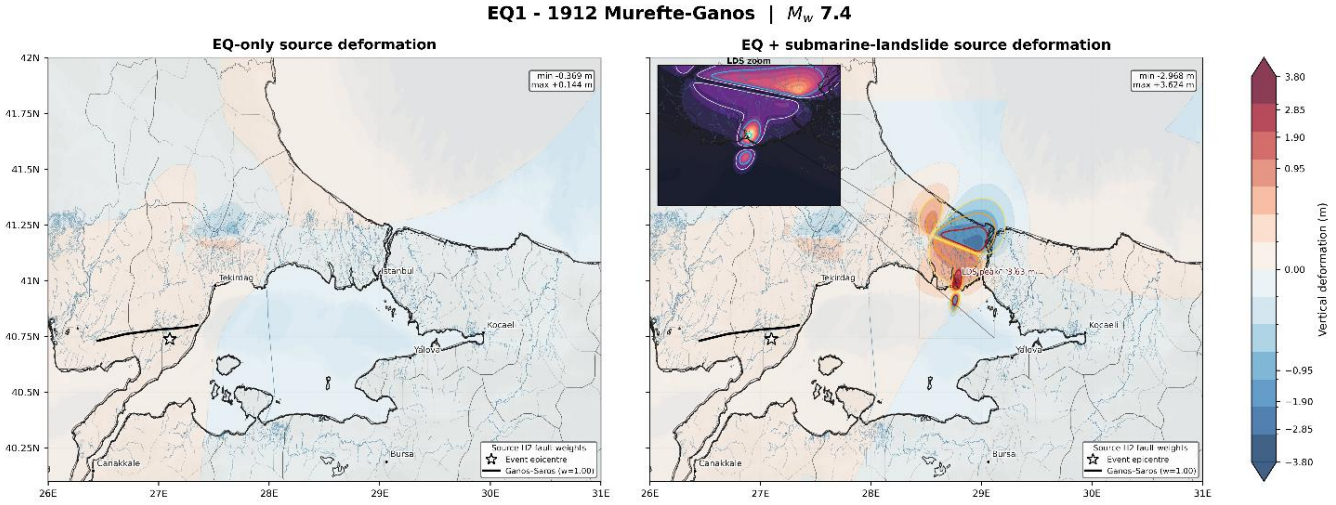

Figure 7. Representative EQ-only and EQ+submarine-landslide source-deformation fields for EQ1 (from GeoClaw simulation outputs using GEBCO 2024 bathymetry/topography).

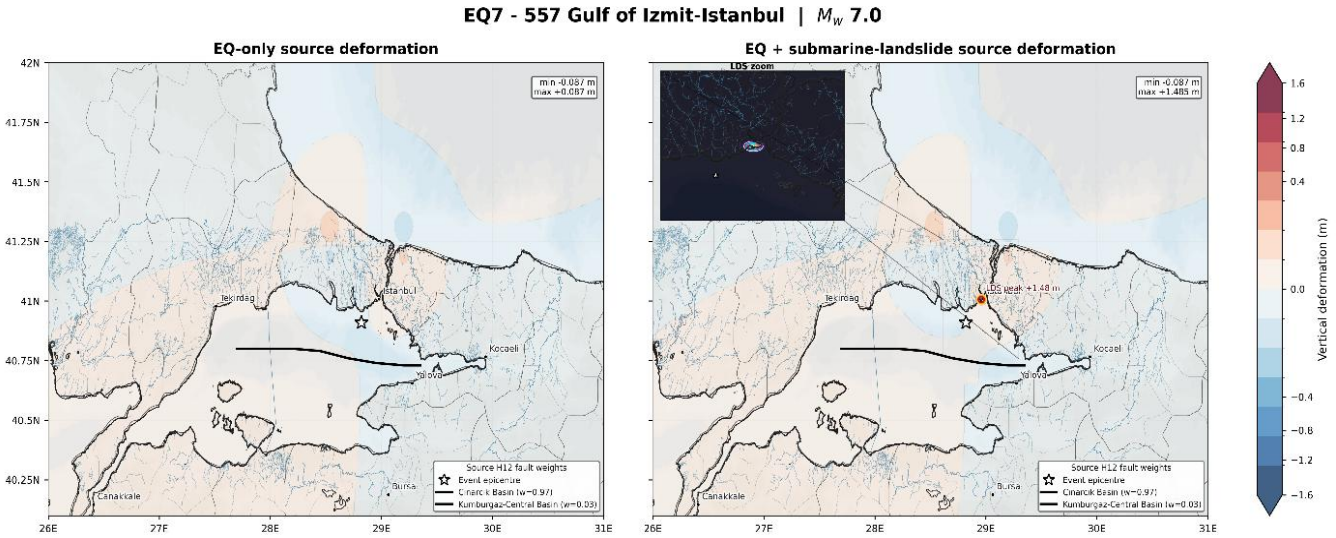

Figure 8. Representative EQ-only and EQ+submarine-landslide source-deformation fields for EQ7 (from GeoClaw simulation outputs using GEBCO 2024 bathymetry/topography).

After the source deformations are generated, GeoClaw compile them along with the bathymetry/topography, still-water hydrodynamic equations (Eq. 1 to Eq. 10), finite-volume Riemann-solver fluxes, wetting-drying treatement, boundary conditions and adaptive mesh refinement, and convert them into initial tsunami elevations and propagated through the Marmara basin to obtain maximum tsunami-induced water-height fields as displyaed in the Fig. 9 and Fig. 10 bellow for EQ1 and EQ7 events respectively. As infered from both Fig. 9 and Fig. 10, the maximum water-heights do not simply replicate the initial

https://doi.org/10.5194/egusphere-2026-4280
Preprint. Discussion started: 9 September 2026
© Author(s) 2026. CC BY 4.0 License.

water form, simply wave propagation, local bathymetry, coastal geometry and basin reproductions redistribute the initial source signal, constructing spatially variable maximum responses around the Marmara Sea. At the same time, the chronological behaviour of the selected scenarios was evaluated using first arrival and peack-response time fields as shown in Fig. 11 for EQ1 and Fig. 12 for EQ7. Both figures show that first arrival and maximum response do not necessarly occur at the same time. In some locations, the first noticeable tsunami waaves early, while the largest response occurs later due to wave reflection, basin resonance, focusing and repeated interactions within the semi-enclosed Marmara basin.

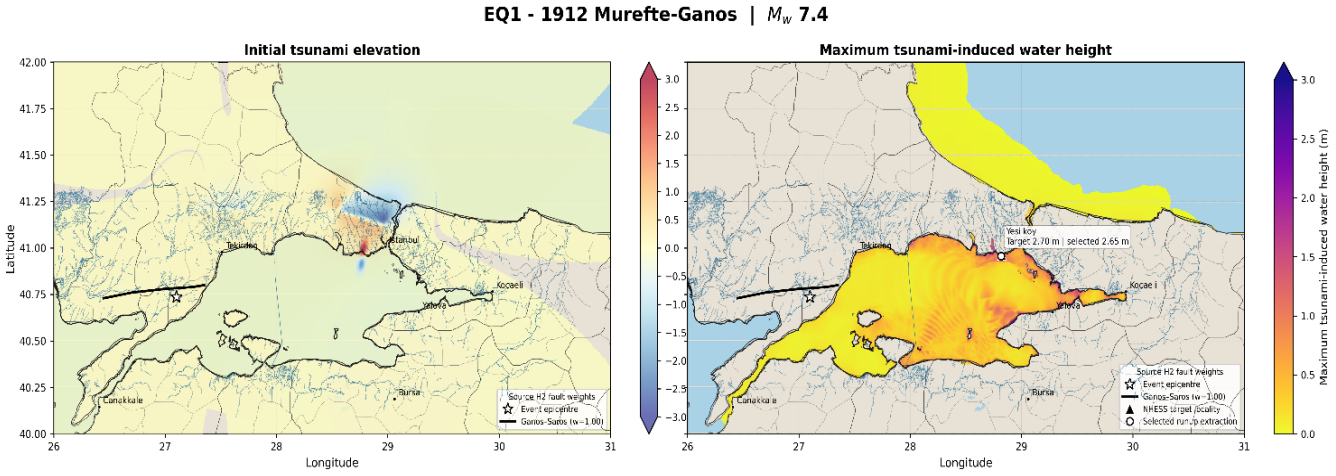

Figure 9. Initial tsunami elevation and maximum tsunami-induced water height for EQ1 (from GeoClaw simulation outputs using GEBCO 2024 bathymetry/topography).

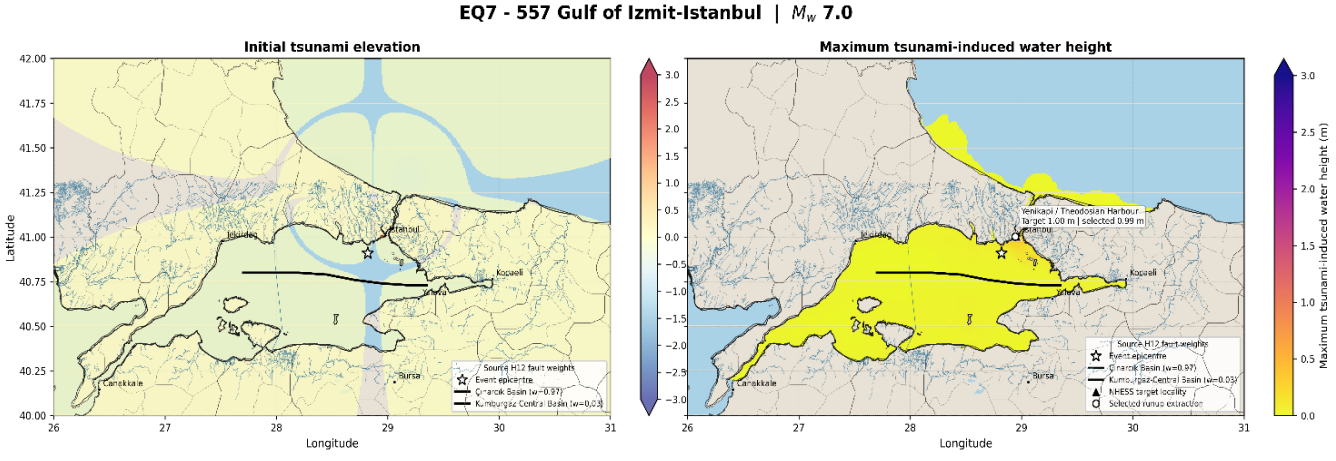

Figure 10. Initial tsunami elevation and maximum tsunami-induced water height for EQ7 (from GeoClaw simulation outputs using GEBCO 2024 bathymetry/topography).

https://doi.org/10.5194/egusphere-2026-4280
Preprint. Discussion started: 9 September 2026
© Author(s) 2026. CC BY 4.0 License.

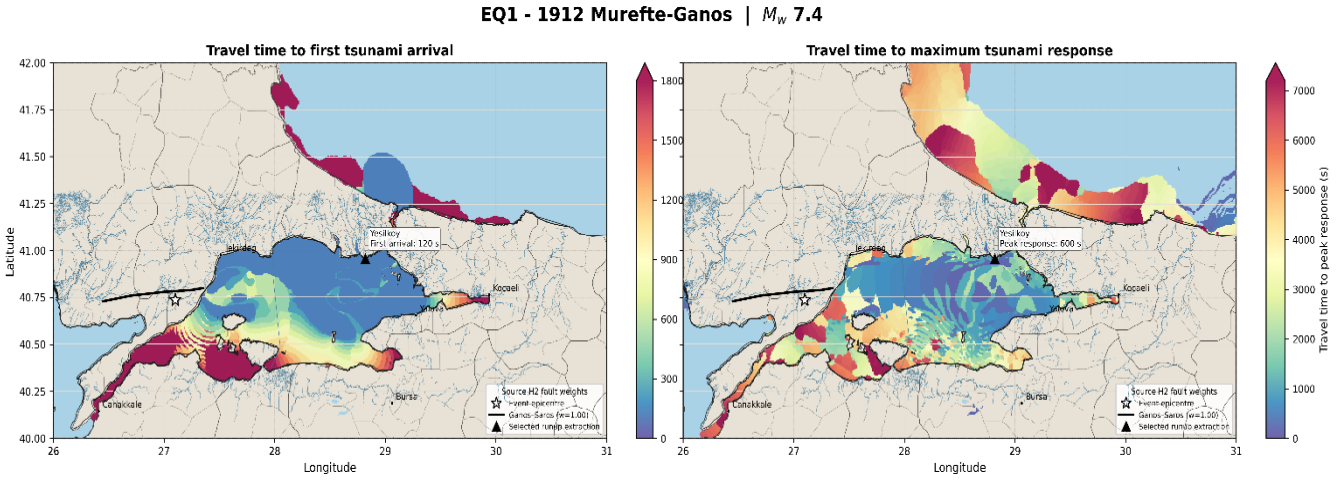

Figure 11. Travel time to first tsunami arrival and to maximum tsunami response for EQ1 (from GeoClaw simulation outputs using GEBCO 2024 bathymetry/topography).

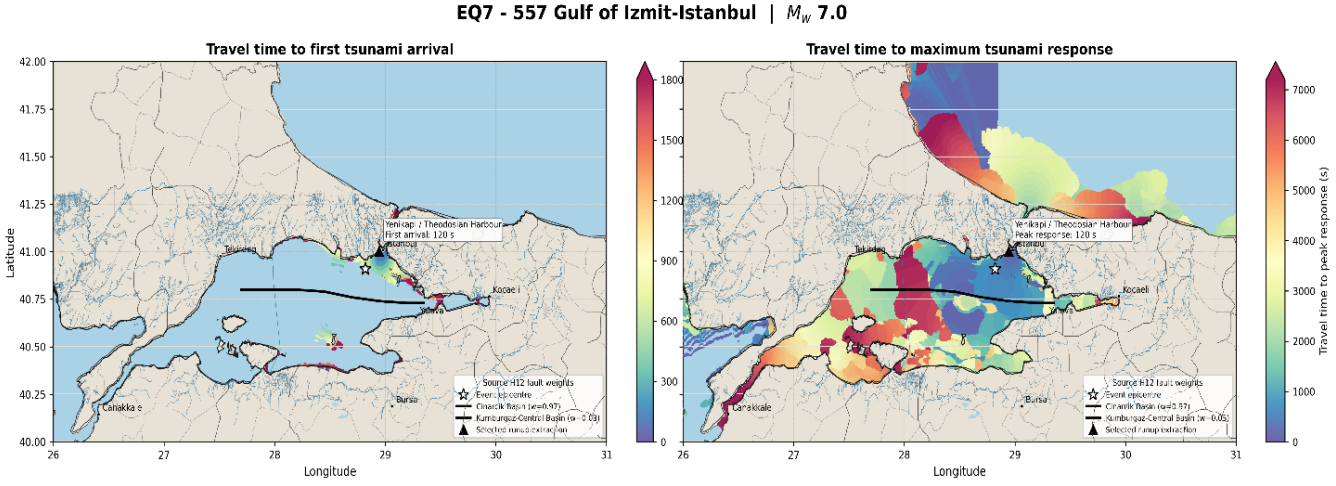

Figure 12. Travel time to first tsunami arrival and to maximum tsunami response for EQ7 (from GeoClaw simulation outputs using GEBCO 2024 bathymetry/topography).

To examine the local hydrodynamic response at target locations and connect the spatial fields with time-dependent tsunami demand, we extracted gauge-level time histories for gauges displayed in the Fig. 4 and display for typical gauges of the EQ1 (Fig.13 to Fig. 17) and EQ7 (Fig. 18 to Fig. 22). The gauge histories confirm that sea-surface anomaly, total water depth, flow speed and momentum flux are not essentially maximized simultaneously. This is imperative for infrastructure applications because bridge and coastal-structure demand depend not only on water elevation but also on flow velocity, momentum flux and directionality.

https://doi.org/10.5194/egusphere-2026-4280
Preprint. Discussion started: 9 September 2026
© Author(s) 2026. CC BY 4.0 License.

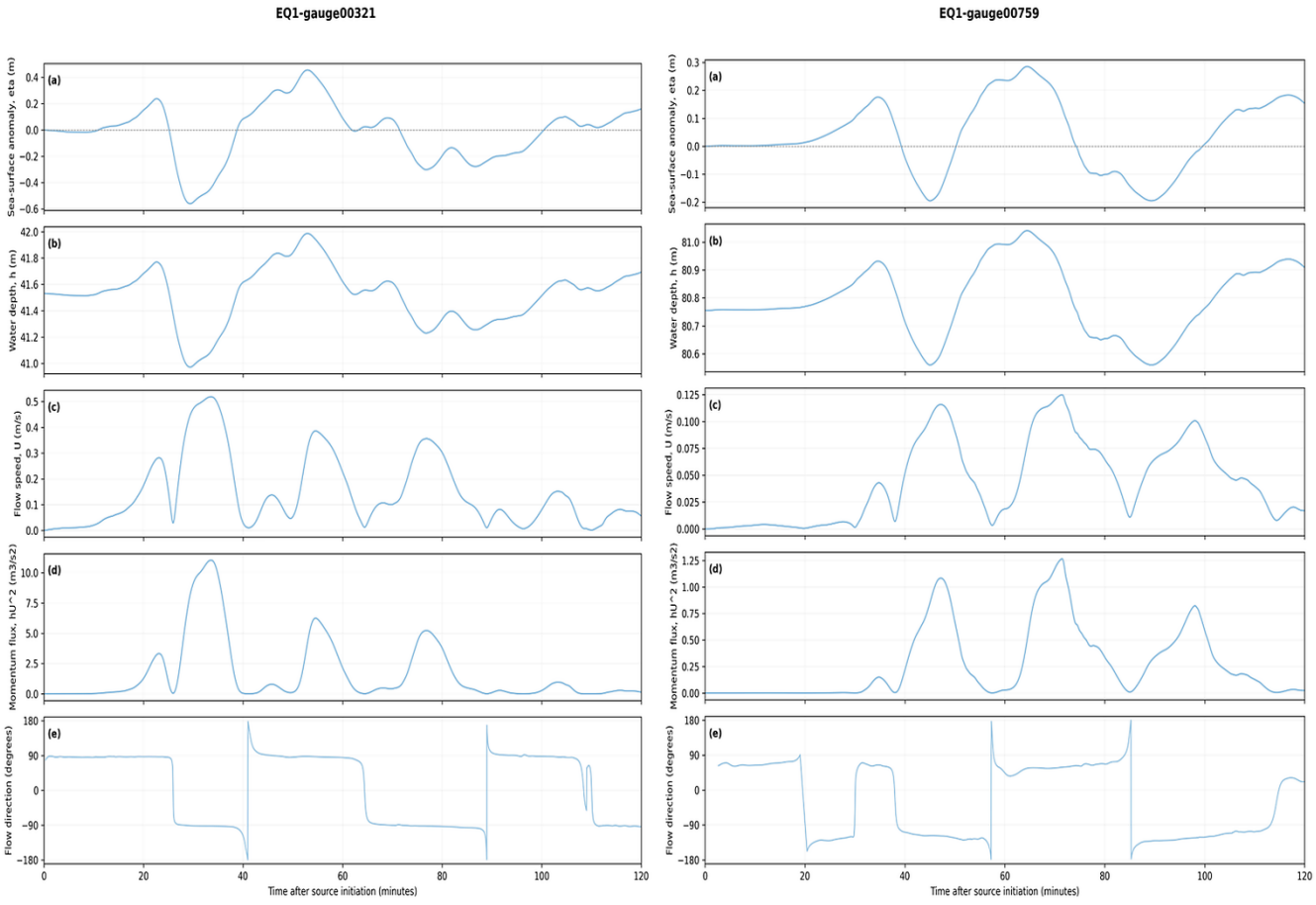

Figure 13. Representative benchmark-gauge hydrodynamic histories for EQ1.

Considering hydrodynamic histories variations across gauges (gauges locations presented in Fig. 4), ensemble responses were plotted for EQ1 as displayed in the Fig. 14 to Fig. 17 and Fig. 19 to Fig. 22 for EQ7. These figures demonstrate how sea surface anomaly envelopes, strongly vary among gauges. The near-zero median does not imply absence of tsunami response; rather, it indicates that positive crests and negative drawdowns occur at different locations and partly cancel in the median summary (Fig. 14 and Fig. 19). Regarding the water depth displayed in the Fig. 15 and Fig. 20, it mirrors the bathymetric setting of the retained gauges and globally represent the full water column above the seabed, with the tsunami perturbation superimposed on the local bathymetry. The momentum flux itself from the Fig. 16 and Fig. 22 gives more direct indicator of the hydrodynamic demand than water elevation alone, mainly its peak that identify time windows where the tsunami may produce stronger horizontal loading on coastal or bridge components. The flow-speed envelops reveal that velocity demand can remain spatially variable even in case of moderate sea-surface anomaly. All these supports the use of multiple tsunami intensity measures instead of relying only on run-up or maximum water elevation.

https://doi.org/10.5194/egusphere-2026-4280
Preprint. Discussion started: 9 September 2026
© Author(s) 2026. CC BY 4.0 License.

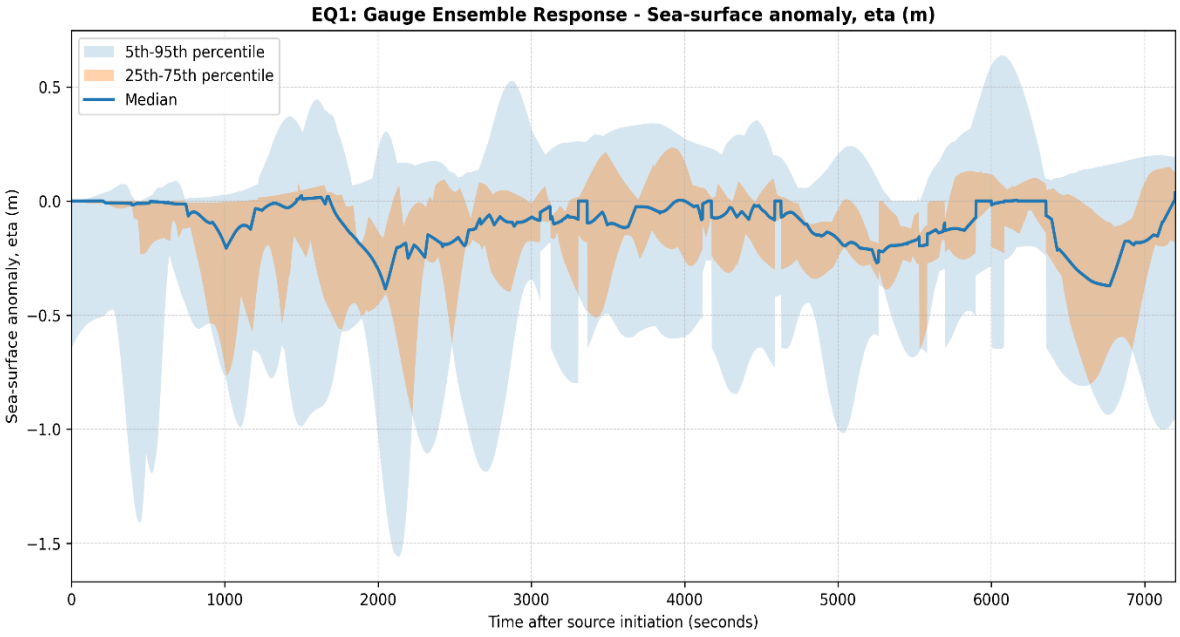

Figure 14. Gauge ensemble response for EQ1: sea-surface anomaly, η.

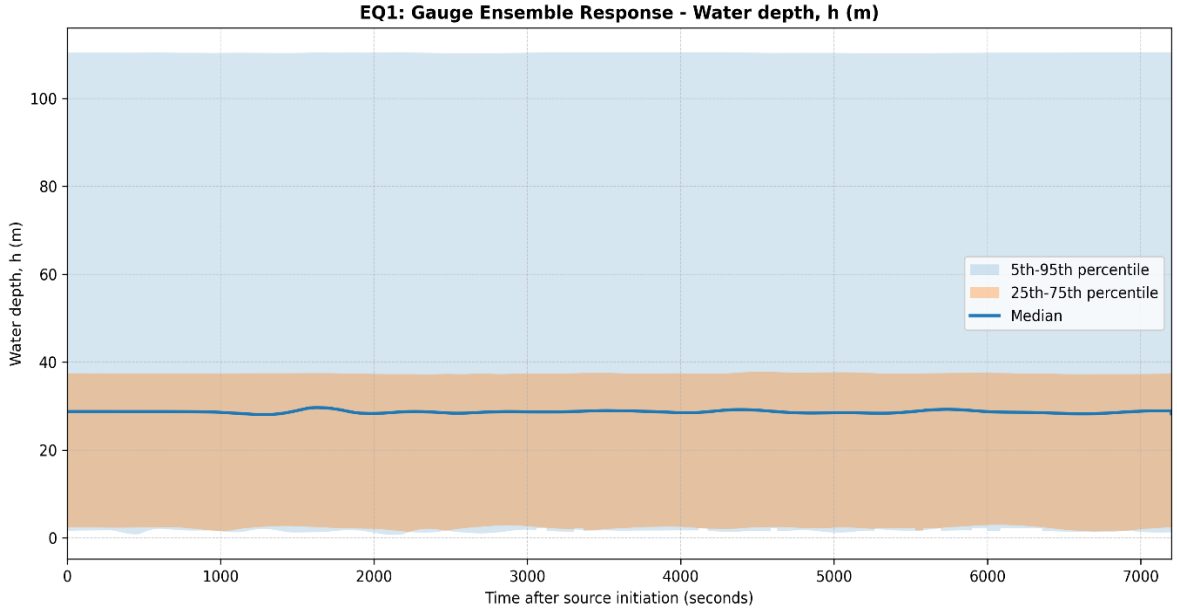

Figure 15. Gauge ensemble response for EQ1: water depth, h.

https://doi.org/10.5194/egusphere-2026-4280
Preprint. Discussion started: 9 September 2026
© Author(s) 2026. CC BY 4.0 License.

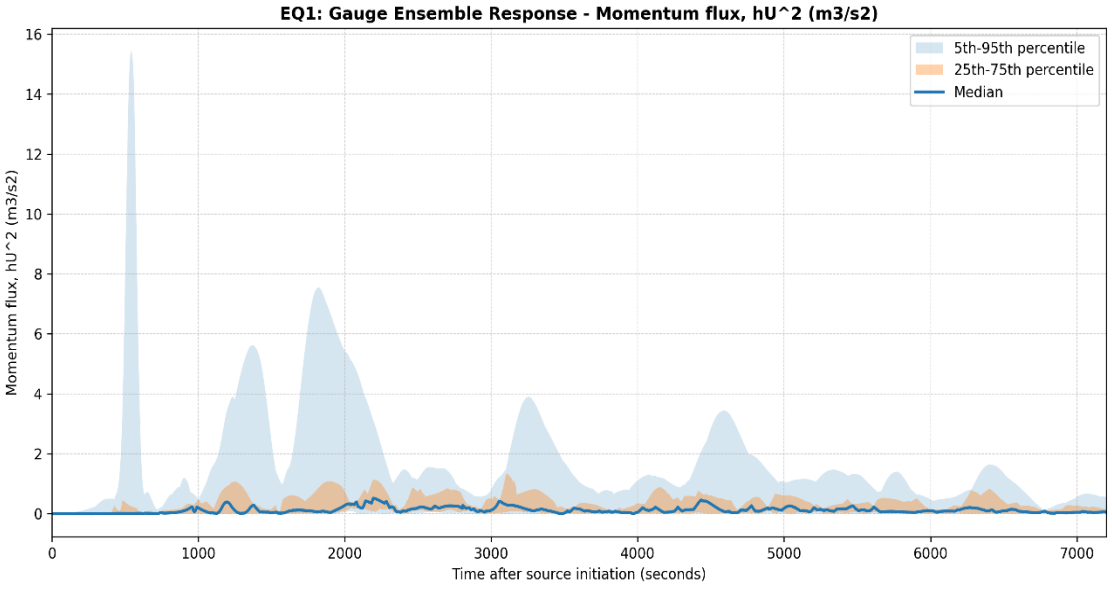

Figure 16. Gauge ensemble response for EQ1: momentum flux, hU^2.

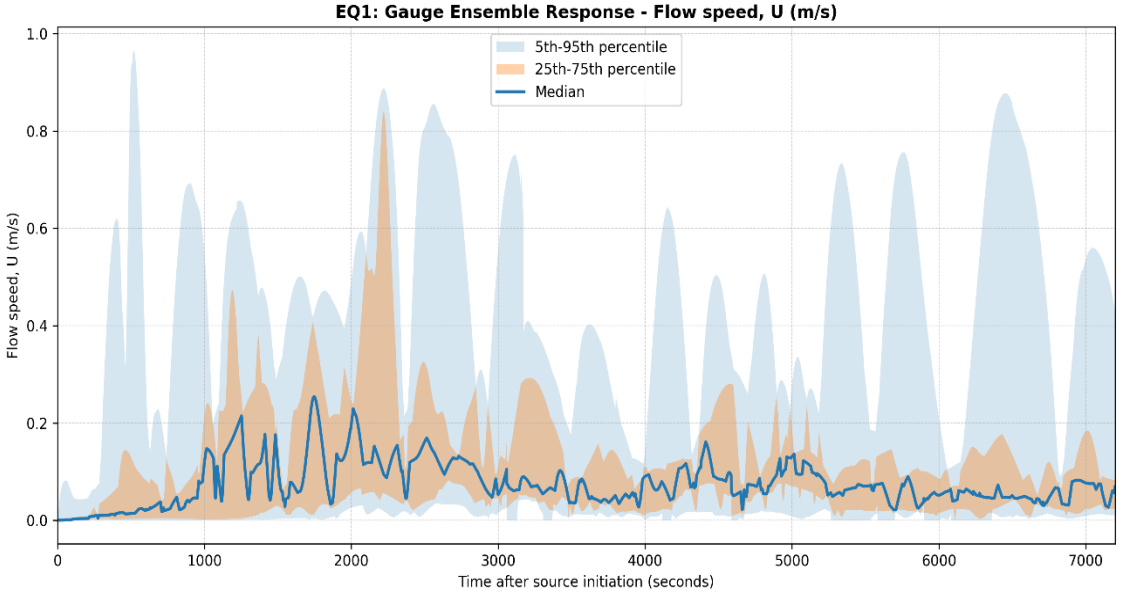

Figure 17. Gauge ensemble response for EQ1: flow speed, U.

https://doi.org/10.5194/egusphere-2026-4280
Preprint. Discussion started: 9 September 2026
© Author(s) 2026. CC BY 4.0 License.

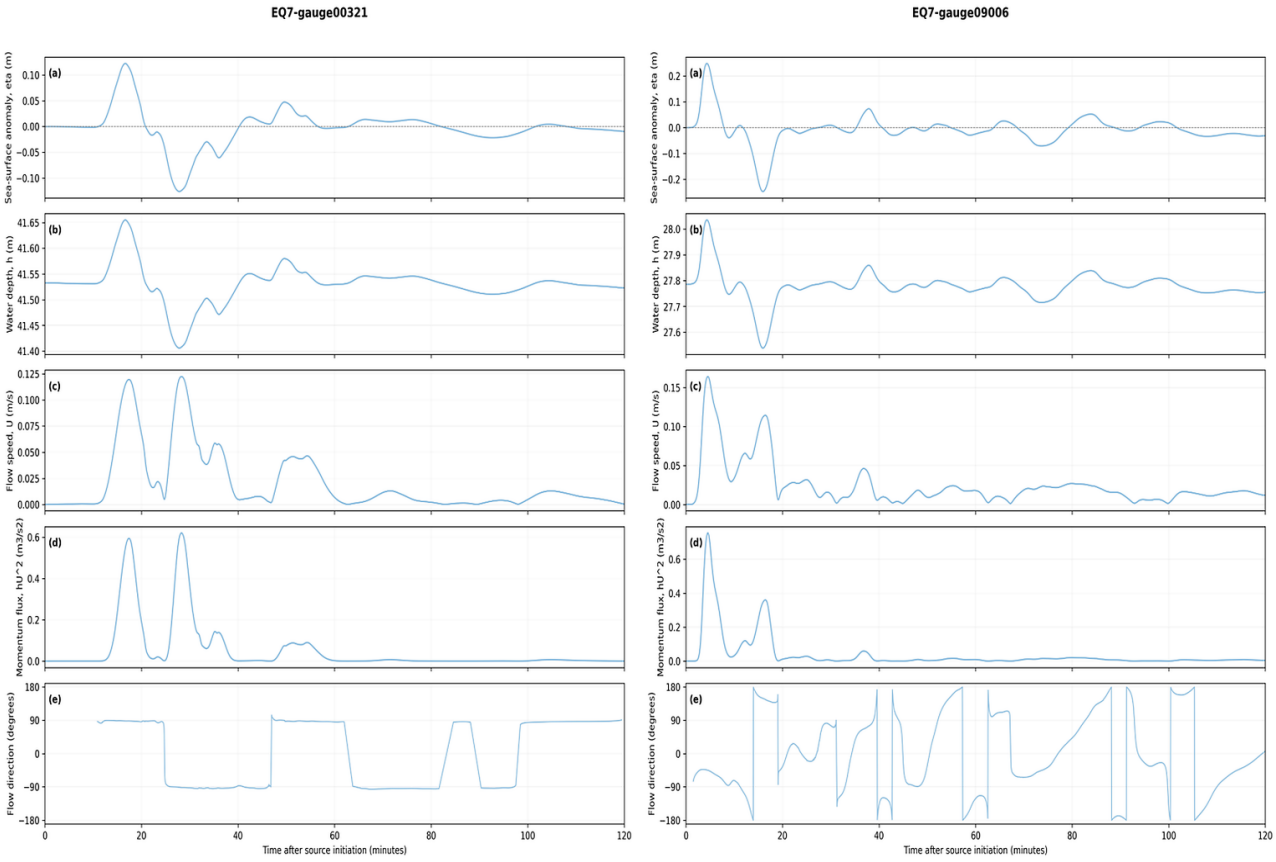

Figure 18. Representative benchmark-gauge hydrodynamic histories for EQ7.

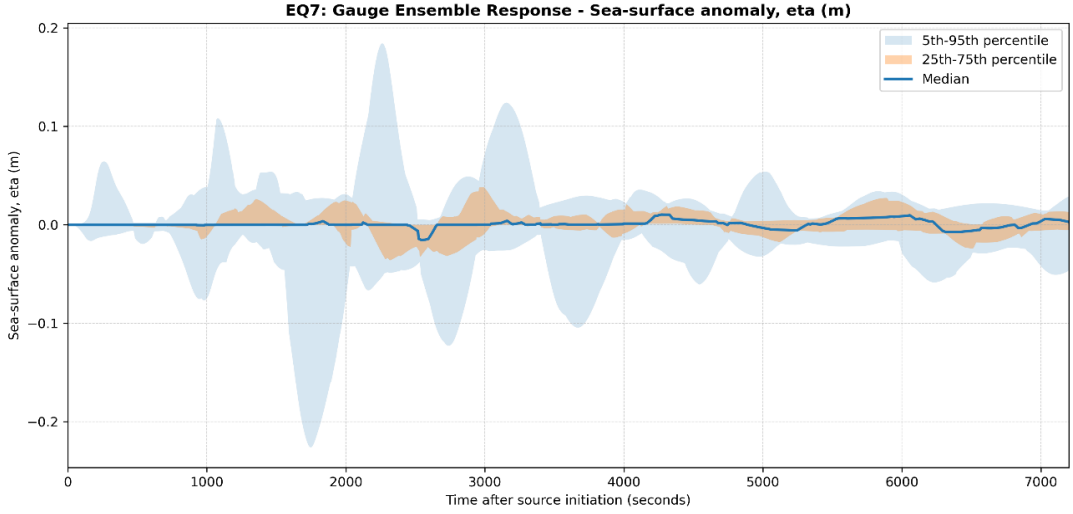

Figure 19. Gauge ensemble response for EQ7: sea-surface anomaly, η.

https://doi.org/10.5194/egusphere-2026-4280
Preprint. Discussion started: 9 September 2026
© Author(s) 2026. CC BY 4.0 License.

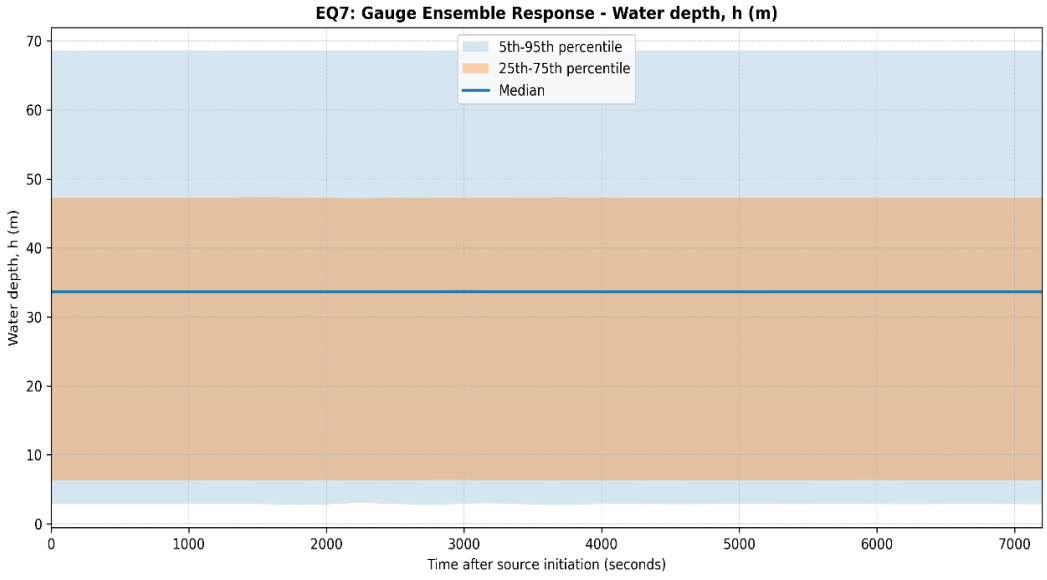

Figure 20. Gauge ensemble response for EQ7: water depth, h.

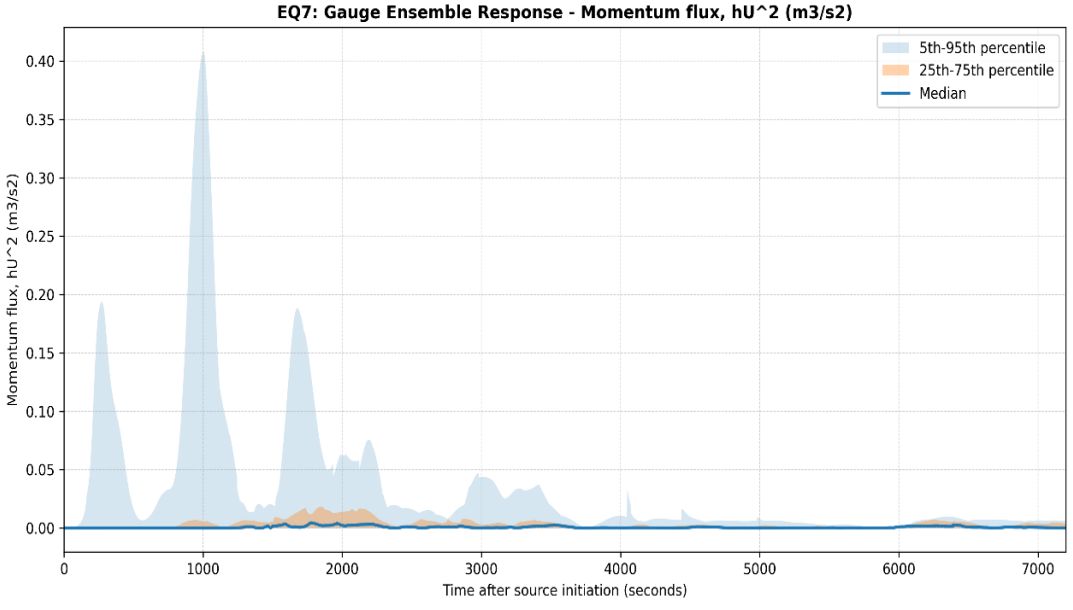

Figure 21. Gauge ensemble response for EQ7: momentum flux, hU^2.

https://doi.org/10.5194/egusphere-2026-4280
Preprint. Discussion started: 9 September 2026
© Author(s) 2026. CC BY 4.0 License.

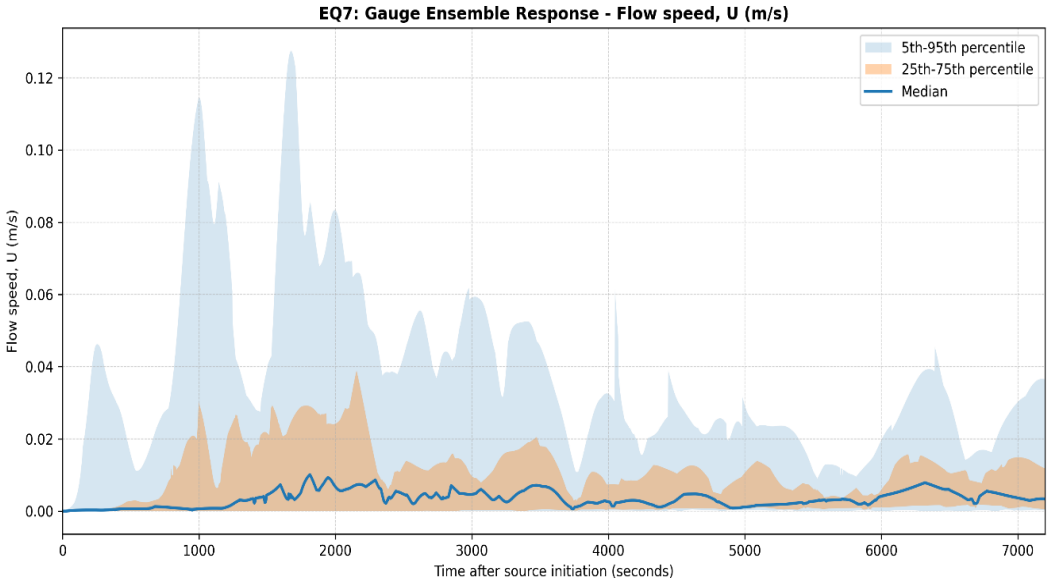

Figure 22. Gauge ensemble response for EQ7: flow speed, U.

From a global view of the seven selected events, they were compared using cross-event timing and intensity summaries. As displayed in the Fig. 23 and Fig. 24, the normalized intensity fingerprint highlights strong event-to-event variability among the seven selected scenarios. The EQ1 dominate the dynamic response metrics, while EQ7 produce the largest median water depth, and EQ3 showing delayed first arrival, while EQ2–EQ8 produce the most persistent tsunami signals. The arrival-time and tsunami duration distributions from Fig. 25 show that source location and basin geometry strongly influence disturb the timing of tsunami impact. Events with nearby sources may produce earlier arrivals, while more distributed responses can produce wider timing ranges across gauges. From a combined views from Fig. 23, Fig. 24 and Fig. 25, it can be concluded that the most rapid event is not necessarily the most hydrodynamically severe. As example, EQ1 shows relatively strong median flow-speed and momentum-flux indicators, whereas other events may show larger total water-depth values (eg. EQ7), because their retained gauges are in deeper bathymetric settings.

https://doi.org/10.5194/egusphere-2026-4280
Preprint. Discussion started: 9 September 2026
© Author(s) 2026. CC BY 4.0 License.

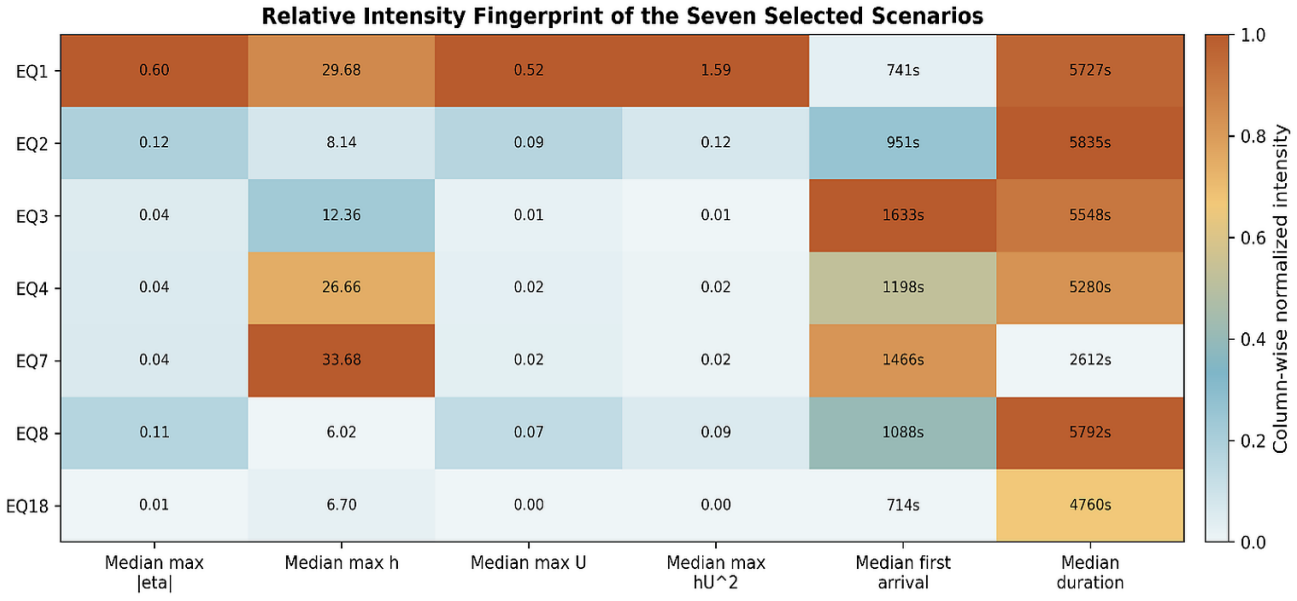

Figure. 23. Cross-event relative intensity fingerprint of the selected Marmara events.

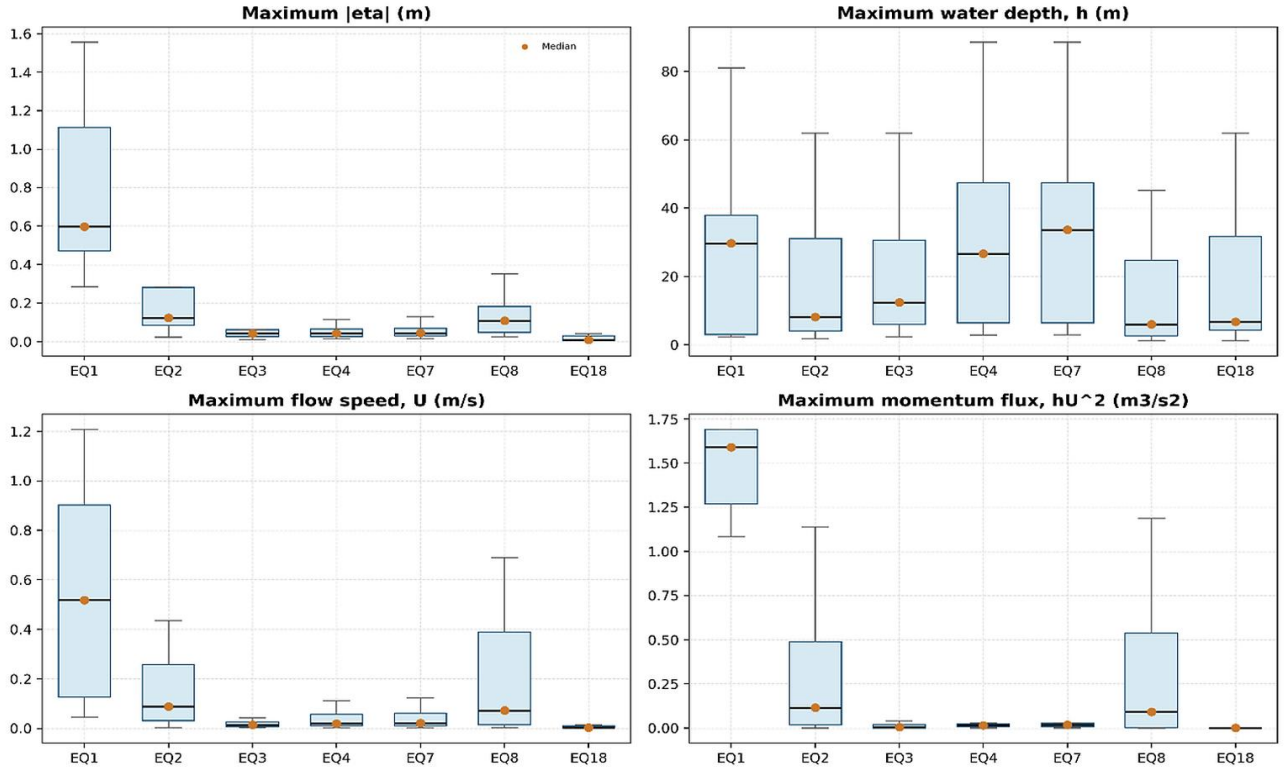

Figure 24. Cross-event comparison of tsunami intensity measure distribution across the selected Marmara events.

https://doi.org/10.5194/egusphere-2026-4280
Preprint. Discussion started: 9 September 2026
© Author(s) 2026. CC BY 4.0 License.

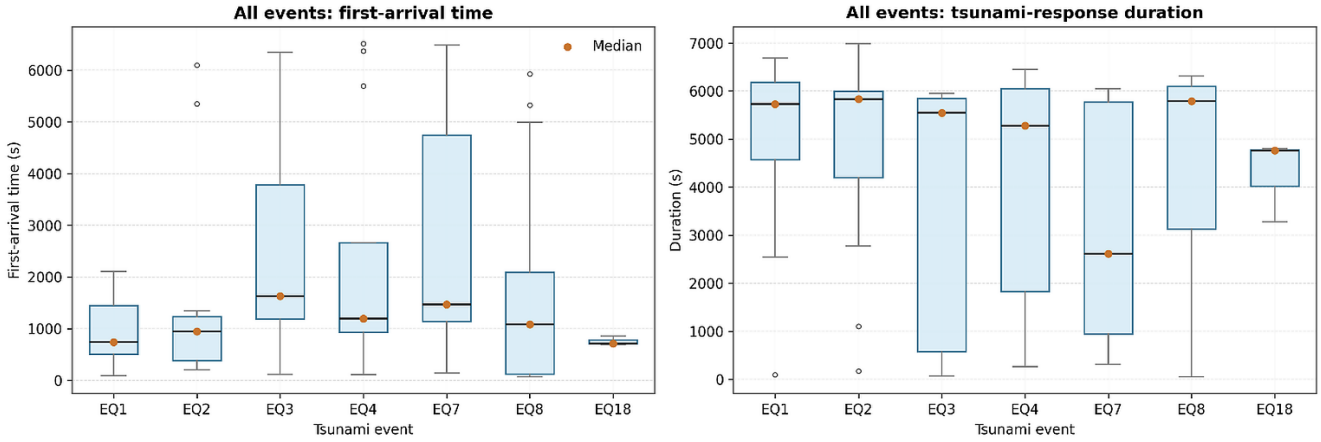

Figure 25. Cross-event comparison of tsunami arrival times and durations across the selected Marmara events.

Overall, the results demonstrate how the selected Marmara tsunami scenarios differed in source deformation, initial elevation, propagation timing, gauge-level hydrodynamic response and cross-event intensity. Moreover, the 20-lane diagnostics show that, the final seven-event benchmark set was obtained through an event-aware source-selection procedure, with most scenarios supported by the L03 spine and selected cases necessitating alternative earthquake-plus-landslide arrangements. This provides a visible foundation for the subsequent discussion of historical consistency, modelling uncertainty and infrastructure-relevant tsunami demand.

5. Discussion

5.1. Historical benchmark consistency and scenario selection

Objectively, this study is not to claim that one single tsunami source can fully describe the Marmara tsunami events, but to establish a reproducible scenario-selection workflow controlled by historical runup-evidence. From the total of 22-event catalogue, seven with well reported site-based runups were restrained and passed 20-lane sources/model comparison. This comes from a context where Marmara tsunami reality is sparse, spatially uneven and often expressed through place names or narrative descriptions instead of modern instrumental records. Consequently, the final selected run-ups should be interpreted as standard-consistent simulation outputs, and not as raw offshore gauge samples.

The validation results show that the final selected scenarios reproduce the reported Altınok et al. (2011) (NHESS) run-up targets with low residuals. Nevertheless, this agreement should not be read as proof that the exact historical sources are exclusively resolved, rather it demonstrates that the selected source–propagation combinations are physically plausible and consistent with the available historical constraints. This distinction is important for data-sparse near-field basins, where ancient run-up observations offer important constraints but cannot completely fix rupture geometry, landslide geometry, or local shoreline amplification.

https://doi.org/10.5194/egusphere-2026-4280
Preprint. Discussion started: 9 September 2026
© Author(s) 2026. CC BY 4.0 License.

5.2. Role of earthquake and submarine-landslide source components

The deformations maps displayed in Fig. 7 and Fig. 8 establish the evidence that submarine-landslide components behave as a localized perturbation superimposed on the broader co-seismic deformation, and the deformations ranges proving the earthquake-plus-landslide (EQ+LDS) contributing as a varying amplification and changing the source amplitude envelope with spatial distribution in an event-dependent manner. This supports the use of event-aware source choice rather than a single source family for all historical cases. Besides, the final selected lane structure supports this interpretation, with nearly all events reproduced by L03 NHESS-based source backbone, with exception to only EQ8 that is produced by L01-lane earthquake-plus-landslide (LDS) configuration. This proves that a common source-construction logic can reproduce most benchmark targets, while at least one event can benefit from a totally different source representation. Such behaviour is predictable in the Marmara Sea, where tsunami generation may involve both tectonic displacement and localized submarine slope processes.

5.3. Hydrodynamic response and infrastructure relevance

Reading from the gauge-level outputs (Fig. 13 to Fig. 23), it's clear that the initial source deformation only can't reproduce tsunami response. Instead, it requires the effects of bathymetry, coastal geometry, basin reflection and repeated wave interactions to redistribute the initial disturbance and generate spatially variable maximum water-heigh, arrival-time, and peak-response fields. It's important also to notice that first arrival and maximum response do not necessarily occur at the same time, which is relevant for warning interpretation and for infrastructure demand modelling.

The results from gauges time-histories explain that the sea-surface anomaly, water depth, flow speed, momentum flux, and directionality are not maximized at the same time. This approves that tsunami demand for bridges and coastal transport assets cannot be characterized by run-up or maximum water elevation alone. Instead, flow speed and momentum-flux proxies offer further information on probable horizontal loading windows, whereas arrival and duration metrics aid define the time windows required for subsequent nonlinear time-history analysis. The chosen gauge outputs thus provide a bridge between historical tsunami reconstruction and infrastructure-oriented hazard assessment.

5.4. Uncertainty and limitations

For future improvement of this study, it has been identified some uncertainties and limitations that could be considered. These include first, the historical run-up targets affected by location uncertainty, narrative interpretation and differences amid reported coastal effects and modelled proxy points. At other part, there are also the focal mechanisms and source perturbation that are not exclusively constrained for olden and pre-instrumental events. Additionally, depth-average shallow-water equations were considered in the modelling excluding factors such as frequency dispersion, sediment transport (Masaya et al., 2020) and detailed local behaviour geometry, and run-up as well as inundation estimate quality depend also on the resolution and accuracy of the bathymetry/topography data near the coast.

Thought all these limitations do not overturn the workflow; they define its appropriate interpretation. Consequently, the results should be used as historically constrained scenario products and hydrodynamic demand inputs, not as definitive

https://doi.org/10.5194/egusphere-2026-4280
Preprint. Discussion started: 9 September 2026
© Author(s) 2026. CC BY 4.0 License.

reconstructions of unique past tsunami bases. The value of the 20-lane construction is that it exposes these choices instead of hiding them behind a single preferred simulation.

5.5. Transferability

This study established a workflow and methodology that can be transferred to other near-field basins where instrumental tsunami records are sparse, but run-up descriptions, bathymetry, mapped faults and probable source hypothesise are available. Specifically, all labelled lane structures, the separation of physical backbone scenarios from diagnostic alternatives, the explicit run-up validation table and preservation of gauge histories for infrastructure applications could be easily transferred to other case events. That's why the proposed approach is well useful for not only historical tsunami reconstruction/validation, but also for risk-informed planning in coastal regions where multiple source mechanisms may contribute to hazard.

6. Conclusions

This study developed a physics-based and benchmark-constrained GeoClaw workflow to reconstruct historical Marmara Sea tsunami scenarios. From a total of 22-events historical-tsunami catalogue, seven with of reported run-up target by (Altınok et al., 2011) were retained and evaluated through 20-lane of source/model comparison (the corresponding lane-control and scaling matrices are documented in the **Appendix A**). The workflow connects source deformation, bathymetry/topography, tsunami propagation, maximum water height fields, arrival and peak-response timing, gauge histories and bridge-ready hydrodynamic outputs. At the end of the selection process, the best seven-scenario set records strong agreement with the historical run-up benchmarks, with RMSE = 0.024 m, MAE = 0.019 m, maximum absolute residual = 0.048m, and MAPE = 1.1%, with all seven absolute percent errors below 10%. The lane comparison also confirmed the insufficiency of wet-gauge positive crests as direct run-up proxies, although the selected simulation results provide more appropriate benchmark-consistent representation of the reported historical local positions.

At other part, the source diagnostics show that most selected cases are represented by the L03 NHESS-based source backbone, while EQ8 is better epitomised by the L01 earthquake-plus-landslide configuration. This indicates that a common source-construction logic explains most historical run-up targets, but that event-specific earthquake-plus-landslide source representation is needed for at least one scenario. The EQ+LDS fields change the deformation range considerably and introduce localized source perturbations without simply replacing the broader earthquake-controlled deformation pattern.

Finally, the propagated tsunami fields and gauge histories reveal that initial elevation, maximum water height, first arrival, peak-response time, flow speed, and momentum flux define different aspects of tsunami impact. These quantities are not maximized simultaneously and therefore should be interpreted together, especially when the outputs are used for bridge or coastal-infrastructure demand assessment. The resulting gauge histories provide direct input for subsequent nonlinear time-history analysis of bridge systems exposed to earthquake-tsunami sequences.

Opening the debate to further improvement of this study, it's important to indicate some limitations that emended from the main workflow. Otherwise, future study could consider solving uncertainty in historical run-up locations, simplified representation of submarine landslide contributions, source-parameter uncertainty Sopacı and Özacar, (2023),

https://doi.org/10.5194/egusphere-2026-4280
Preprint. Discussion started: 9 September 2026
© Author(s) 2026. CC BY 4.0 License.

bathymetric/topographic resolution, and the use of depth-averaged shallow-water modelling. However, despite these limitations, the labelled lane structure makes the modelling choices transparent and reproducible. The proposed workflow can be extended to other data-sparse near-field basins where historical evidence and modern numerical modelling must be combined for tsunami hazard and infrastructure-risk assessment.

https://doi.org/10.5194/egusphere-2026-4280
Preprint. Discussion started: 9 September 2026
© Author(s) 2026. CC BY 4.0 License.

Appendix. A Source-lane design, parameter controls, and event-specific scaling.

This appendix documents the internal structure of the 20-lane Marmara tsunami modelling ensemble. The figures identify which lanes modified source-family assumptions, earthquake and landslide scaling factors, numerical/model-control terms, and source-geometry parameters. These diagnostic matrices support the reproducibility of the lane-selection process used.

Binary control matrix showing which modelling components were modified or controlled in each lane of the 20-lane source/model ensemble. Dark cells indicate that the component was explicitly touched by the lane, while light cells indicate the base setup was retained. Please noted that all lanes' notations with NHESS prefix are referring to Altınok et al. (2011) and mainly its reported runups.

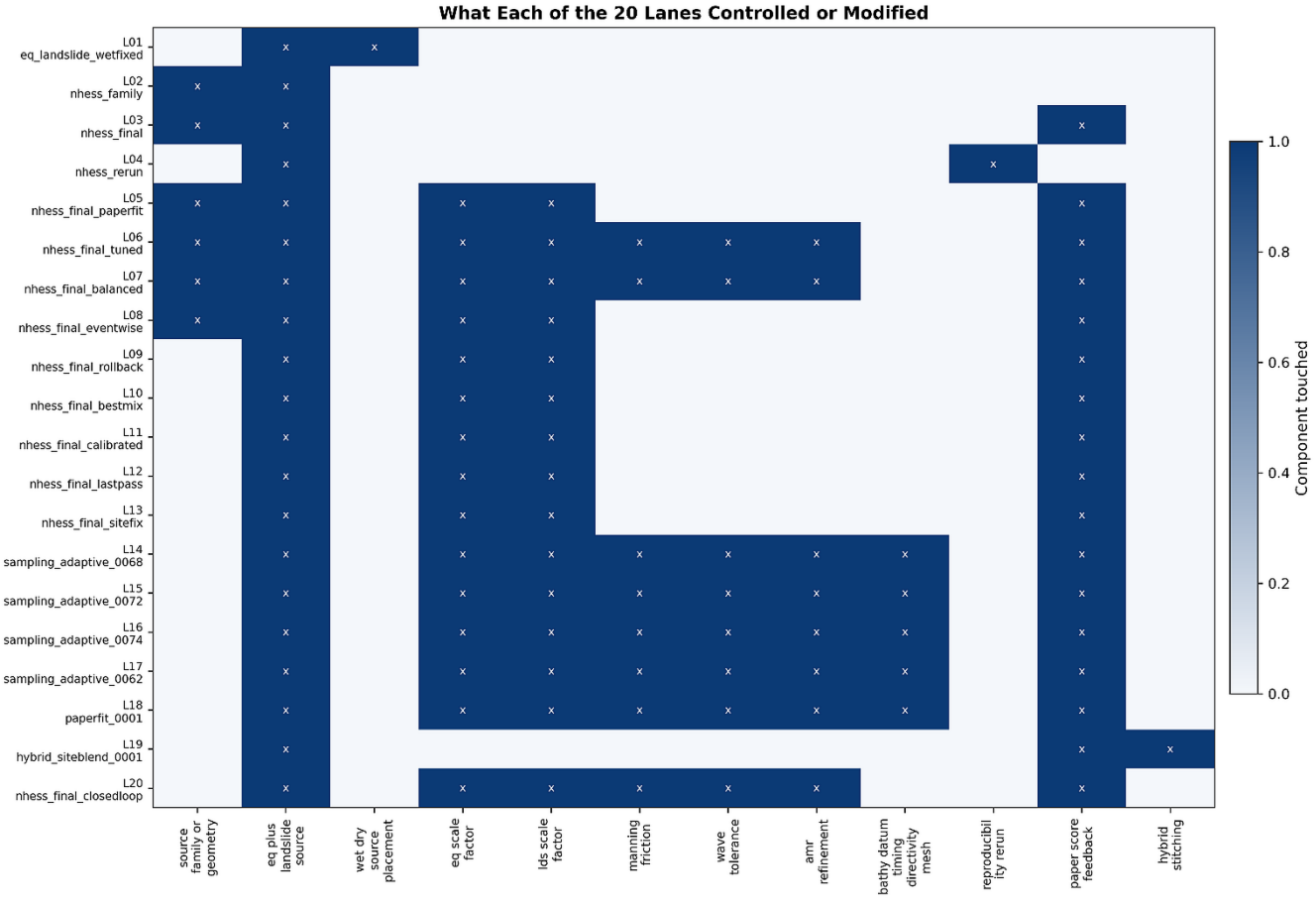

Figure A1. Source-lane control matrix for the 20-lane Marmara tsunami ensemble.

In the Fig 2, it can be seen the heatmap of earthquake-source scale factors applied by event and lane. Cells labelled "base" indicate the reference source setup, while numerical cells indicate explicit source-scaling factors used in the corresponding lane. Regarding Fig. 3, it presents the heatmap of submarine-landslide source scale factors applied by event and lane. The

https://doi.org/10.5194/egusphere-2026-4280
Preprint. Discussion started: 9 September 2026
© Author(s) 2026. CC BY 4.0 License.

figure documents where landslide amplitude or source intensity was retained at the base value and where event-specific scale factors were introduced.

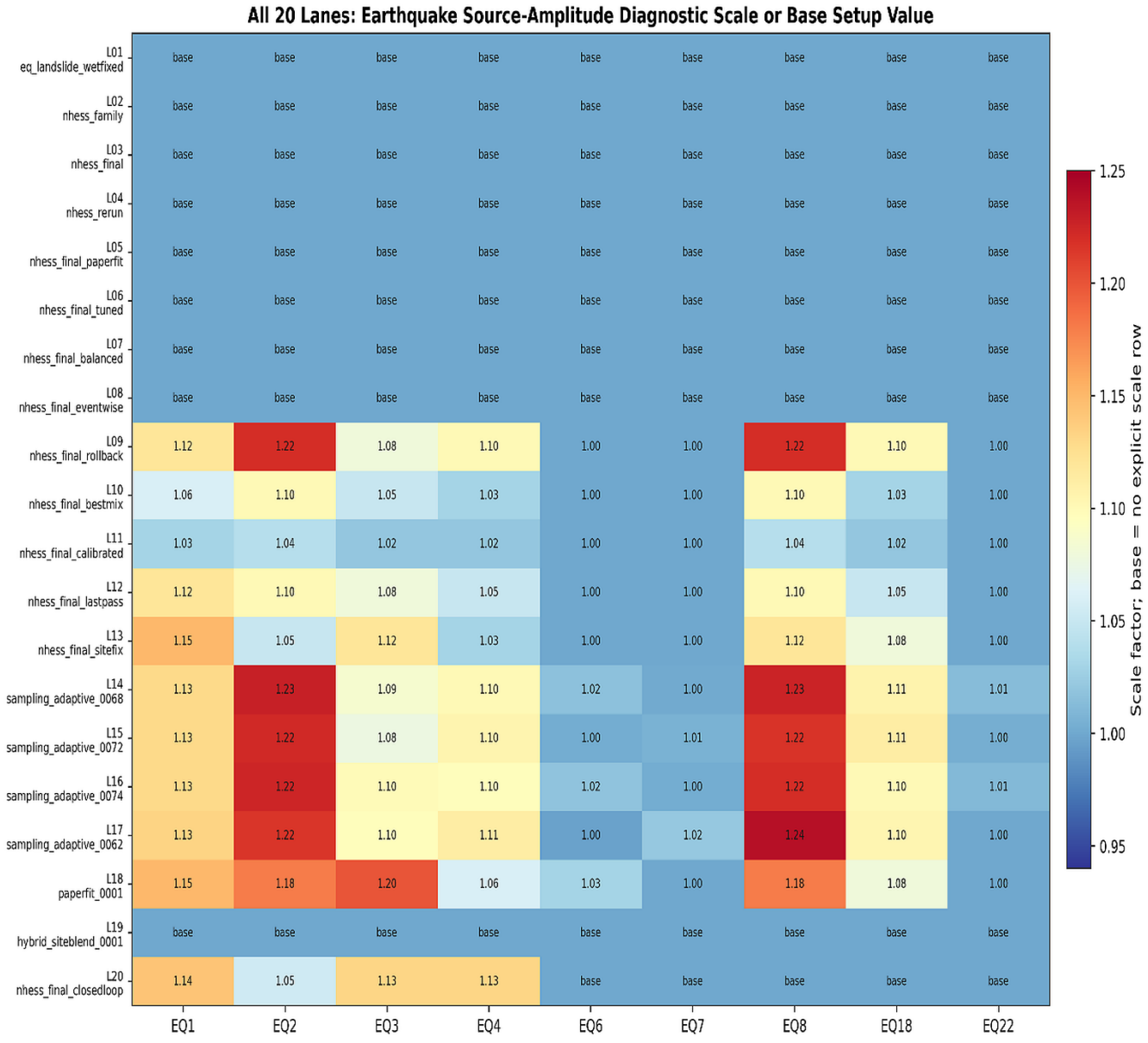

Figure A2. Event-wise earthquake-source scaling factors across the 20 lanes.

https://doi.org/10.5194/egusphere-2026-4280
Preprint. Discussion started: 9 September 2026
© Author(s) 2026. CC BY 4.0 License.

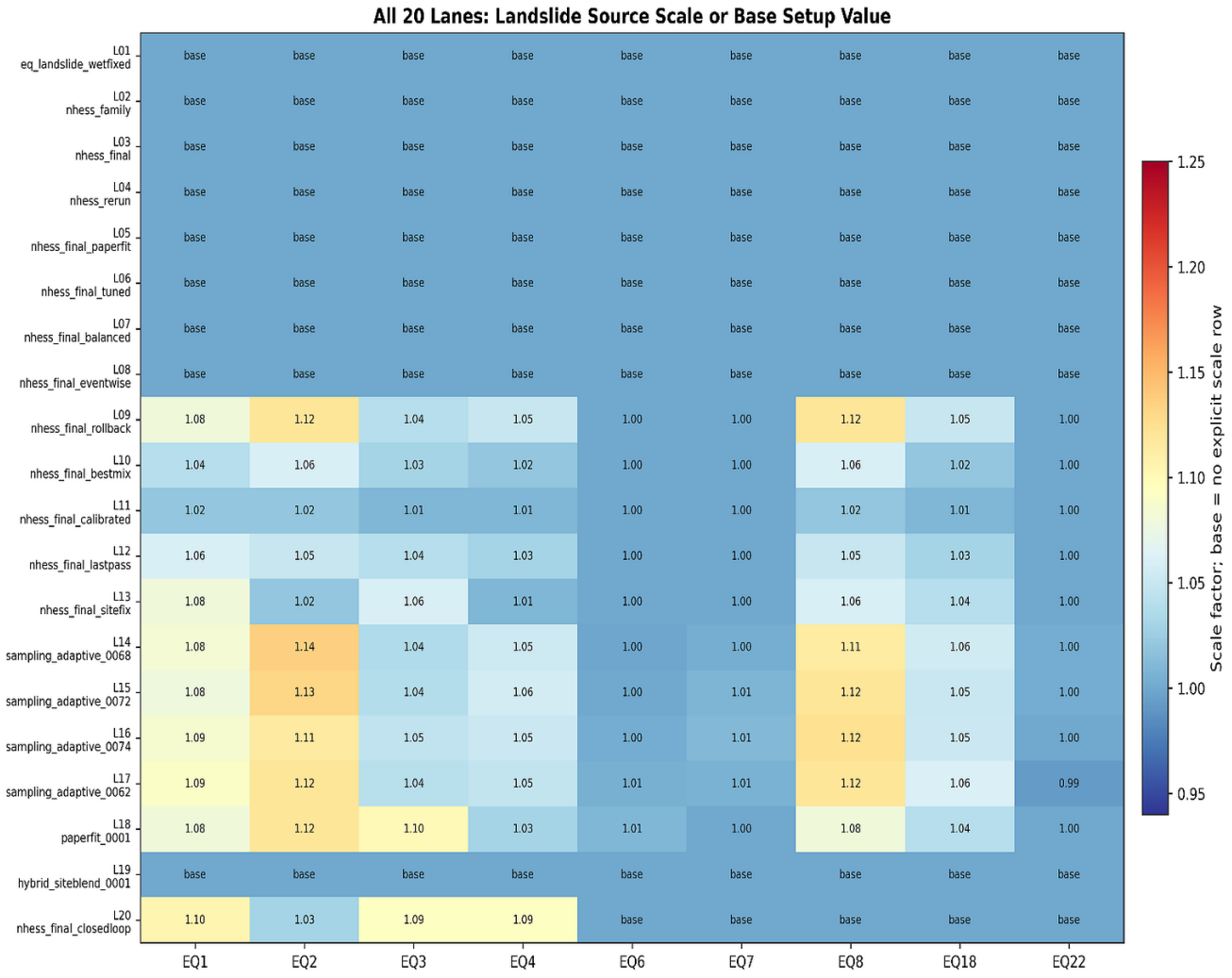

Figure A3. Event-wise landslide-source scaling factors across the 20 lanes.

Code availability

The tsunami simulations were completed with GeoClaw/Clawpack, an open-source finite-volume tsunami and geophysical-flow modelling framework (Berger et al., 2011; LeVeque et al., 2011; Team, 2026). The developed scripts and workflow, including the source-catalogue preparation, seven-scenario validation table, the 20-lane sources/model comparison, selected processed intensity measures, environment/requirement files, the manuscript-table exports as well as figure-reproduction scripts are stored in the Zenodo repository *Marmara Tsunami Physics-Based Scenario Selection: Code and Data Package*, version v1.0 (Djima and Zulfikar, 2026), https://doi.org/10.5281/zenodo.21467453. Additional raw simulation folders and very large intermediate outputs that are not included in the archive can be requested from the corresponding author where storage and licensing constraints permit.

https://doi.org/10.5194/egusphere-2026-4280
Preprint. Discussion started: 9 September 2026
© Author(s) 2026. CC BY 4.0 License.

Data availability

The processed data required to reproduce the main results of this study are archived in the Zenodo repository *Marmara Tsunami Physics-Based Scenario Selection: Code and Data Package*, version v1.0 (Djima and ZULFIKAR, 2026), https://doi.org/10.5281/zenodo.21467453. The archive includes the selected seven-event catalogue, the full 22-event catalogue where available, lane dictionary, selected-scenario validation metrics, processed deformation, runup, travel-time, maximum-water-height and gauge-history summaries, manuscript-table CSV exports, supplementary lane matrices, and available figure outputs. The historical tsunami/runup constraints used for benchmark comparison are based mainly on the Marmara/Turkish tsunami catalogue of Altınok et al. (2011). Bathymetry/topography data used for the modelling were obtained from the GEBCO 2024 grid (GEBCO Compilation Group, 2024). Fault/source information and supporting geological constraints were compiled from the literature cited in the manuscript. Large raw GeoClaw frame outputs, complete non-selected lane output folders, and restricted or very large third-party bathymetry/topography products are not redistributed; they are documented in the large-file manifest and can be provided where licensing and storage constraints permit.

Competing interests

The authors declare that they have no competing interests.

Acknowledgements

The authors acknowledge Gebze Technical University and Istanbul Technical University for academic support. The authors also acknowledge the open-source GeoClaw/Clawpack community and the providers of bathymetric, topographic, and geospatial datasets used in this study.

Author contributions

Author contributions. WGD designed the study, prepared the source catalogue and numerical workflow, performed the GeoClaw simulations, processed the validation and figure outputs, and wrote the manuscript. ACZ supervised the research, contributed to the scientific framing and interpretation, and reviewed and revised the manuscript.

Financial support

This research received partial financial support from Islamic Development Bank, IsDB Merit Scholarship Program for Member Countries under PhD Program/ID: 2023-639079.

References

Aksoy, E., Meghraoui, M., and Toussaint, R.: The slip deficit along the North Anatolian Fault (Turkey) in the Marmara Sea: Insights from paleoseismicity, seismicity and geodetic data, , https://doi.org/10.5194/egusphere-egu2020-8809, 2020.

Altınok, Y., Alpar, B., Özer, N., and Aykurt, H.: Revision of the tsunami catalogue affecting Turkish coasts and surrounding regions, Nat. Hazards Earth Syst. Sci., 11, 273–291, https://doi.org/10.5194/nhess-11-273-2011, 2011.

American Society of Civil Engineers: Minimum Design Loads and Associated Criteria for Buildings and Other Structures, ASCE/SEI 7-16, American Society of Civil Engineers, Reston, VA, https://doi.org/10.1061/9780784414248, 2017.

https://doi.org/10.5194/egusphere-2026-4280
Preprint. Discussion started: 9 September 2026
© Author(s) 2026. CC BY 4.0 License.

Aránguiz, R., Urra, L., Okuwaki, R., and Yagi, Y.: Development and application of a tsunami fragility curve of the 2015 tsunami in Coquimbo, Chile, Nat. Hazards Earth Syst. Sci., 18, 2143–2160, https://doi.org/10.5194/nhess-18-2143-2018, 2018.

Armijo, R., Pondard, N., Meyer, B., Uçarkuş, G., de Lépinay, B. M., Malavieille, J., Dominguez, S., Gustcher, M., Schmidt, S., Beck, C., Çağatay, N., Çakır, Z., Imren, C., Eriş, K., Natalin, B., Özalaybey, S., Tolun, L., Lefèvre, I., Seeber, L., Gasperini, L., Rangin, C., Emre, O., and Sarıkavak, K.: Submarine fault scarps in the Sea of Marmara pull-apart (North Anatolian Fault): Implications for seismic hazard in Istanbul, Geochem. Geophys. Geosystems, 6, 2004GC000896, https://doi.org/10.1029/2004gc000896, 2005.

Ateş, R.: Earthquake Activity on the North Anatolian Fault Zone, in: Multidisciplinary Approach to Earthquake Prediction, 95–113, https://doi.org/10.1007/978-3-663-14015-3_7, 1982.

Behrens, J.: R7—ASCETE Coupled Earthquake-Tsunami Modelling, in: Mathematics of Planet Earth, 447–452, https://doi.org/10.1007/978-3-031-98115-9_16, 2026.

Berger, M. J., George, D. L., LeVeque, R. J., and Mandli, K. T.: The GeoClaw software for depth-averaged flows with adaptive refinement, Adv. Water Resour., 34, 1195–1206, https://doi.org/10.1016/j.advwatres.2011.02.016, 2011.

Bryant, E.: Earthquake-Generated Tsunami, in: Tsunami, 85–102, https://doi.org/10.1007/978-3-319-06133-7_5, 2014.

Bulkan, S., Vannucchi, P., Gasperini, L., Polonia, A., and Cavozzi, C.: Modelling tectonic deformation along the North-Anatolian Fault in the Sea of Marmara, Tectonophysics, 794, 228612, https://doi.org/10.1016/j.tecto.2020.228612, 2020.

Dao, M. H. and Tkalich, P.: Tsunami propagation modelling – a sensitivity study, Nat. Hazards Earth Syst. Sci., 7, 741–754, https://doi.org/10.5194/nhess-7-741-2007, 2007.

Davies, G. and Griffin, J.: The 2018 Australian probabilistic tsunami hazard assessment: hazard from earthquake generated tsunamis, https://doi.org/10.11636/record.2018.041, 2018.

Dimova, L., Raykova, R., Armigliato, A., Pagnoni, G., and Tinti, S.: Modelling of earthquake-induced tsunami in the Eastern Mediterranean Region, in: AIP Conference Proceedings, 120024, https://doi.org/10.1063/1.5091282, 2019.

Djima, W. G. and ZULFIKAR, A. C.: Marmara Tsunami Physics-Based Scenario Selection: Code and Data Package, , https://doi.org/10.5281/zenodo.21467453, 2026.

Ergün, M., Özel, E., and Sari, C.: Structure of the Marmara Sea Basin in the North Anatolian Fault Zone, in: Rifted Ocean-Continent Boundaries, 309–326, https://doi.org/10.1007/978-94-011-0043-4_17, 1995.

Galán Pérez, D., Aniel-Quiroga, I., Gallego, A., Aguirre-Ayerbe, I., González, M., Quetzalcóatl, O., Álvarez-Gómez, J. A., and Pedraz, L.: The TSUSY Database: a global database of historical tsunami events and a tsunami-occurrence criterion based on historical earthquakes, Nat. Hazards Earth Syst. Sci., 26, 2415–2436, https://doi.org/10.5194/nhess-26-2415-2026, 2026.

Gasperini, L. and Polonia, A.: Active segments along the North Anatolian Fault system in the Sea of Marmara, , https://doi.org/10.5194/egusphere-egu23-1250, 2023.

Gasperini, L., Zaniboni, F., Armigliato, A., Tinti, S., Pagnoni, G., Özeren, M. S., Ligi, M., Natali, F., and Polonia, A.: Tsunami potential source in the eastern Sea of Marmara (NW Turkey), along the North Anatolian Fault system, Landslides, 19, 2295–2310, https://doi.org/10.1007/s10346-022-01929-0, 2022.

https://doi.org/10.5194/egusphere-2026-4280
Preprint. Discussion started: 9 September 2026
© Author(s) 2026. CC BY 4.0 License.

George, D. L.: Augmented Riemann solvers for the shallow water equations over variable topography with steady states and inundation, J. Comput. Phys., 227, 3089–3113, https://doi.org/10.1016/j.jcp.2007.10.027, 2008.

Gökaşan, E., Gazioğlu, C., Alpar, B., Yücel, Z., Ersoy, Ş., Gündoğdu, O., Yaltırak, C., and Tok, B.: Evidence of NW extension of the North Anatolian Fault Zone in the Marmara Sea: a new interpretation of the Marmara Sea (İzmit) earthquake on 17 August 1999, Geo-Mar. Lett., 21, 183–199, https://doi.org/10.1007/s00367-001-0088-0, 2001.

González-Riancho, P., Aliaga, B., Hettiarachchi, S., González, M., and Medina, R.: A contribution to the selection of tsunami human vulnerability indicators: conclusions from tsunami impacts in Sri Lanka and Thailand (2004), Samoa (2009), Chile (2010) and Japan (2011), Nat. Hazards Earth Syst. Sci., 15, 1493–1514, https://doi.org/10.5194/nhess-15-1493-2015, 2015.

Hébert, H., Schindelé, F., Altınok, Y., Alpar, B., and Gazioğlu, C.: Tsunami hazard in the Marmara Sea (Turkey): a numerical approach to discuss active faulting and impact on the Istanbul coastal areas, Mar. Geol., 215, 23–43, https://doi.org/10.1016/j.margeo.2004.11.006, 2005.

Hébert, H., Didenkulova, I., Fritz, H. M., and Papadopoulos, G. A.: Preface: New challenges for tsunami science: understanding tsunami processes to improve mitigation and enhance early warning, Nat. Hazards Earth Syst. Sci., 16, 1855–1857, https://doi.org/10.5194/nhess-16-1855-2016, 2016.

Karabacak, V., Uysal, I. T., and al., et: Supplemental Material: When did the North Anatolian fault reach southern Marmara, Turkey?, , https://doi.org/10.1130/geol.s.17118797.v1, 2021.

Karabacak, V., Uysal, I. T., Yildirim, G., and Sançar, T.: Supplemental Material: When did the North Anatolian fault reach southern Marmara, Turkey?, , https://doi.org/10.1130/G49726.1, 2022.

Kaya-Eken, T., Ogawa, Y., Usui, Y., Kasaya, T., Tunçer, M. K., Honkura, Y., Oshiman, N., Matsushima, M., and Siripunvaraporn, W.: Supplemental Material: 3-D electromagnetic imaging of highly deformed fluid-rich weak zones and locked section of the North Anatolian fault beneath the Marmara Sea, , https://doi.org/https://doi.org/10.1130/G52995.1, 2026.

LeVeque, R. J., George, D. L., and Berger, M. J.: Tsunami modelling with adaptively refined finite volume methods, Acta Numer., 20, 211–289, https://doi.org/10.1017/s0962492911000043, 2011a.

LeVeque, R. J., George, D. L., and Berger, M. J.: Tsunami modelling with adaptively refined finite volume methods, Acta Numer., 20, 211–289, https://doi.org/10.1017/s0962492911000043, 2011b.

Masaya, R., Suppasri, A., Yamashita, K., Imamura, F., Gouramanis, C., and Leelawat, N.: Investigating beach erosion related with tsunami sediment transport at Phra Thong Island, Thailand, caused by the 2004 Indian Ocean tsunami, Nat. Hazards Earth Syst. Sci., 20, 2823–2841, https://doi.org/10.5194/nhess-20-2823-2020, 2020.

McHugh, C., Seeber, L., Cormier, M.-H., and Hornbach, M.: Submarine Paleoseismology Along Populated Transform Boundaries: The Enriquillo-Plantain-Garden Fault, Canal du Sud, Haiti, and the North Anatolian Fault, Marmara Sea, Turkey, Oceanography, 27, 118–131, https://doi.org/10.5670/oceanog.2014.47, 2014.

Meghraoui, M., Toussaint, R., and Aksoy, M. E.: Stress evolution and slip deficit on the North Anatolian Fault (Turkey) in the Marmara Sea: insights from paleoseismicity, seismicity and geodetic data, , https://doi.org/10.5194/egusphere-egu22-11676, 2022.

Meral Ozel, N., Ocal, N., Ahmet Cevdet, Y., Dogan, K., and Mustafa, E.: Tsunami hazard in the eastern Mediterranean and its connected seas: Towards a Tsunami warning center in Turkey, Soil Dyn. Earthq. Eng., 31, 1080, https://doi.org/10.1016/j.soildyn.2011.03.001, 2011.

https://doi.org/10.5194/egusphere-2026-4280
Preprint. Discussion started: 9 September 2026
© Author(s) 2026. CC BY 4.0 License.

Nakano, M., Citak, S., and Kalafat, D.: Focal mechanism determinations of earthquakes along the North Anatolian fault, beneath the Sea of Marmara and the Aegean Sea, Earth Planets Space, 67, 159, https://doi.org/10.1186/s40623-015-0330-z, 2015.

Nosov, M. A. and Skachko, S. N.: Nonlinear tsunami generation mechanism, Nat. Hazards Earth Syst. Sci., 1, 251–253, https://doi.org/10.5194/nhess-1-251-2001, 2001.

Oglesby, D. D. and Mai, P. M.: Fault geometry, rupture dynamics and ground motion from potential earthquakes on the North Anatolian Fault under the Sea of Marmara, Geophys. J. Int., 188, 1071–1087, https://doi.org/10.1111/j.1365-246x.2011.05289.x, 2012.

Okada, Y.: Surface deformation due to shear and tensile faults in a half-space, Bull. Seismol. Soc. Am., 75, 1135–1154, https://doi.org/10.1785/bssa0750041135, 1985.

Okada, Y.: Internal deformation due to shear and tensile faults in a half-space, Bull. Seismol. Soc. Am., 82, 1018–1040, https://doi.org/10.1785/bssa0820021018, 1992.

Omira, R., Baptista, M. A., Leone, F., Matias, L., Mellas, S., Zourarah, B., Miranda, J. M., Carrilho, F., and Cherel, J.-P.: Performance of coastal sea-defense infrastructure at El Jadida (Morocco) against tsunami threat: lessons learned from the Japanese 11 March 2011 tsunami, Nat. Hazards Earth Syst. Sci., 13, 1779–1794, https://doi.org/10.5194/nhess-13-1779-2013, 2013.

Oncel, Ali. O. and Wilson, T.: Evaluation of earthquake potential along the Northern Anatolian Fault Zone in the Marmara Sea using comparisons of GPS strain and seismotectonic parameters, Tectonophysics, 418, 205–218, https://doi.org/10.1016/j.tecto.2006.02.006, 2006.

Ozener, H., Aktug, B., Yilmaz, O., Sabuncu, A., Gelin, B., Uçan, K. A., Turgut, B., and Batur, M.: Investigating the Earthquake Cycle along Marmara Sea Region of North Anatolian Fault by means of seismo-geodetic observations, , https://doi.org/10.5194/egusphere-egu2020-21829, 2020.

PAPADOPOULOS, G. A., DASKALAKI, E., FOKAEFS, A., and GIRALEAS, N.: TSUNAMI HAZARD IN THE EASTERN MEDITERRANEAN SEA: STRONG EARTHQUAKES AND TSUNAMIS IN THE WEST HELLENIC ARC AND TRENCH SYSTEM, J. Earthq. Tsunami, 04, 145–179, https://doi.org/10.1142/s1793431110000856, 2010.

Parsons, T.: Recalculated probability of $M \geq 7$ earthquakes beneath the Sea of Marmara, Turkey, J. Geophys. Res. Solid Earth, 109, 2003JB002667, https://doi.org/10.1029/2003jb002667, 2004.

Paulatto, M., Pinat, T., and Romanelli, F.: Tsunami hazard scenarios in the Adriatic Sea domain, Nat. Hazards Earth Syst. Sci., 7, 309–325, https://doi.org/10.5194/nhess-7-309-2007, 2007.

Pondard, N., Armijo, R., King, G. C. P., Meyer, B., and Flerit, F.: Fault interactions in the Sea of Marmara pull-apart (North Anatolian Fault): earthquake clustering and propagating earthquake sequences, Geophys. J. Int., 171, 1185–1197, https://doi.org/10.1111/j.1365-246x.2007.03580.x, 2007.

Reese, S., Cousins, W. J., Power, W. L., Palmer, N. G., Tejakusuma, I. G., and Nugrahadi, S.: Tsunami vulnerability of buildings and people in South Java – field observations after the July 2006 Java tsunami, Nat. Hazards Earth Syst. Sci., 7, 573–589, https://doi.org/10.5194/nhess-7-573-2007, 2007.

Roger, J. and Hébert, H.: The 1856 Djijelli (Algeria) earthquake and tsunami: source parameters and implications for tsunami hazard in the Balearic Islands, Nat. Hazards Earth Syst. Sci., 8, 721–731, https://doi.org/10.5194/nhess-8-721-2008, 2008.

https://doi.org/10.5194/egusphere-2026-4280
Preprint. Discussion started: 9 September 2026
© Author(s) 2026. CC BY 4.0 License.

Roger, J. H. M., Faugère, Y., Hébert, H., Delepoulle, A., and Dibarboure, G.: First mapping of a tsunami wavefield by SWOT satellite: observation data and preliminary numerical simulation of the 19 May 2023 tsunami near the Loyalty Islands, Nat. Hazards Earth Syst. Sci., 26, 943–954, https://doi.org/10.5194/nhess-26-943-2026, 2026.

Sahal, A., Roger, J., Allgeyer, S., Lemaire, B., Hébert, H., Schindelé, F., and Lavigne, F.: The tsunami triggered by the 21 May 2003 Boumerdès-Zemmouri (Algeria) earthquake: field investigations on the French Mediterranean coast and tsunami modelling, Nat. Hazards Earth Syst. Sci., 9, 1823–1834, https://doi.org/10.5194/nhess-9-1823-2009, 2009.

Sopacı, E. and Özacar, A. A.: Impact of 2019 Mw 5.8 Marmara Sea Earthquake on the seismic cycle of locked North Anatolian Fault segment, Tectonophysics, 859, 229888, https://doi.org/10.1016/j.tecto.2023.229888, 2023.

Synolakis, C. E.: The runup of solitary waves, J. Fluid Mech., 185, 523–545, https://doi.org/10.1017/s002211208700329x, 1987.

Team, C. D.: GeoClaw documentation, 2026.

Tinti, S. and Tonini, R.: The UBO-TSUFD tsunami inundation model: validation and application to a tsunami case study focused on the city of Catania, Italy, Nat. Hazards Earth Syst. Sci., 13, 1795–1816, https://doi.org/10.5194/nhess-13-1795-2013, 2013.

Titov, V. V. and Synolakis, C. E.: Numerical modeling of tidal wave runup, J. Waterw. Port Coast. Ocean Eng., 124, 157–171, https://doi.org/10.1061/(ASCE)0733-950X(1998)124:4(157), 1998.

Tonini, R., Armigliato, A., Pagnoni, G., Zaniboni, F., and Tinti, S.: Tsunami hazard for the city of Catania, eastern Sicily, Italy, assessed by means of Worst-case Credible Tsunami Scenario Analysis (WCTSA), Nat. Hazards Earth Syst. Sci., 11, 1217–1232, https://doi.org/10.5194/nhess-11-1217-2011, 2011a.

Tonini, R., Armigliato, A., Pagnoni, G., Zaniboni, F., and Tinti, S.: Tsunami hazard for the city of Catania, eastern Sicily, Italy, assessed by means of Worst-case Credible Tsunami Scenario Analysis (WCTSA), Nat. Hazards Earth Syst. Sci., 11, 1217–1232, https://doi.org/10.5194/nhess-11-1217-2011, 2011b.

Utkucu, M., Kanbur, Z., Alptekin, Ö., and Sünbül, F.: Seismic behaviour of the North Anatolian Fault beneath the Sea of Marmara (NW Turkey): implications for earthquake recurrence times and future seismic hazard, Nat. Hazards, 50, 45–71, https://doi.org/10.1007/s11069-008-9317-4, 2009.

Watts, P., Grilli, S. T., Kirby, J. T., Fryer, G. J., and Tappin, D. R.: Landslide tsunami case studies using a Boussinesq model and a fully nonlinear tsunami generation model, Nat. Hazards Earth Syst. Sci., 3, 391–402, https://doi.org/10.5194/nhess-3-391-2003, 2003.

Wells, D. L. and Coppersmith, K. J.: New empirical relationships among magnitude, rupture length, rupture width, rupture area, and surface displacement, Bull. Seismol. Soc. Am., 84, 974–1002, https://doi.org/10.1785/bssa0840040974, 1994.

Williams, J. H., Wilson, T. M., Horspool, N., Paulik, R., Wotherspoon, L., Lane, E. M., and Hughes, M. W.: Assessing transportation vulnerability to tsunamis: utilising post-event field data from the 2011 Tōhoku tsunami, Japan, and the 2015 Illapel tsunami, Chile, Nat. Hazards Earth Syst. Sci., 20, 451–470, https://doi.org/10.5194/nhess-20-451-2020, 2020.